

1 **Atmospheric CO₂ estimates for the Miocene to Pleistocene based on foraminiferal $\delta^{11}\text{B}$ at Ocean**
2 **Drilling Program Sites 806 and 807 in the Western Equatorial Pacific**

4 Maxence Guillermic^{1,2}, Sambuddha Misra^{3,4}, Robert Eagle^{1,2}, Aradhna Tripati^{1,2}

8 ¹Department of Atmospheric and Oceanic Sciences, Department of Earth, Planetary, and Space
9 Sciences, Center for Diverse Leadership in Science, Institute of the Environment and Sustainability,
10 University of California – Los Angeles, Los Angeles, CA 90095 USA

11 ²Laboratoire Géosciences Océan UMR6538, UBO, Institut Universitaire Européen de la Mer, Rue
12 Dumont d'Urville, 29280, Plouzané, France

13 ³ Indian Institute of Science, Centre for Earth Sciences, Bengaluru, Karnataka 560012, India

14 ⁴ The Godwin Laboratory for Palaeoclimate Research, Department of Earth Sciences, University of
15 Cambridge, UK

17 *Correspondence to:* Maxence Guillermic (maxence.guillermic@gmail.com) and Aradhna Tripati
18 (atripati@g.ucla.edu)

19 **ABSTRACT**

20 Constraints on the evolution of atmospheric CO₂ levels throughout Earth's history are foundational to
21 our understanding of past variations in climate. Despite considerable effort, records vary in their
22 temporal and spatial coverage and estimates of past CO₂ levels do not always converge, and therefore
23 new records and proxies are valuable. Here we reconstruct atmospheric CO₂ values across major
24 climate transitions over the past 16 million years using the boron isotopic composition ($\delta^{11}\text{B}$) of
25 planktic foraminifera from 89 samples obtained from two sites in the West Pacific Warm Pool, Ocean
26 Drilling Program (ODP) Sites 806 and 807 measured using high-precision multi-collector inductively-
27 coupled plasma mass spectrometry. We compare our results to published data from ODP Site 872,
28 also in the Western Equatorial Pacific, that goes back to 22 million years ago. These sites are in a
29 region that today is near equilibrium with the atmosphere and are thought to have been in equilibrium
30 with the atmosphere for the interval studied. We show that $\delta^{11}\text{B}$ data from this region are consistent
31 with other boron-based studies. The data show evidence for elevated pCO₂ during the Middle
32 Miocene and Early to Middle Pliocene, and reductions in pCO₂ of ~200 ppm during the Middle
33 Miocene Climate Transition, ~250 ppm during Pliocene Glacial Intensification, and ~50 ppm during
34 the Mid-Pleistocene Climate Transition. During the Mid-Pleistocene Transition there is a minimum
35 pCO₂ at MIS 30. Our results are consistent with a coupling between pCO₂, temperature and ice sheet
36 expansion from the Miocene to the late Quaternary.

37
38 **Highlights**

39 In this study, we reconstruct atmospheric pCO₂ using $\delta^{11}\text{B}$ data from ODP Sites 806 and 807 and
40 compare them with ice core data. We therefore apply the same framework to older samples from these
41 sites to create a long-term pH and pCO₂ reconstruction for the past 16 million years, including
42 recalculating pCO₂ for ODP Site 872 from 17 to 22 million years ago. We find major increases in
43 surface water pH and decreases in atmospheric pCO₂ were associated with decreased temperature in
44 the Western Equatorial Pacific, including associated with major episodes of ice sheet expansion in the
45 high latitudes, providing more robust quantitative constraints on the past coupling between pCO₂,
46 temperature, and cryosphere stability.

47
48 **Keywords**

49 Boron isotopes, CO₂, ODP Site 806, ODP Site 807, Miocene, climate

50 **1. Introduction**

51 Due to concerns about the long-term consequences of anthropogenic emissions and associated
52 climate change (IPCC, 2014, 2018), efforts have been made to quantify past atmospheric CO₂ and
53 examine past relationships between CO₂ and temperature. Such data are not only critical for
54 constraining Earth-system sensitivity (Lea, 2004; Lunt et al., 2010; Pagani et al., 2010; Hansen et al.,
55 2012, 2013, Foster and Rohling, 2013; Schmittner et al., 2011; Tierney et al., 2020), but are also of
56 broad interest to contextualize the evolution of climate and geological systems through Earth's history
57 (Tripati et al., 2011; Foster et al., 2017; Tripati and Darby, 2018). However, discrepancies between
58 proxy reconstructions still exist, including for major climate transitions of the Cenozoic. In particular,
59 there remains a pressing need for robust and higher-resolution atmospheric CO₂ records.

60 High-resolution and direct determinations of atmospheric CO₂ are available for the last 800
61 kyr through analysis of air bubbles extracted from ice-cores, but these records are limited to the
62 availability of cores (Petit et al., 1999; Siegenthaler et al., 2005; Lüthi et al., 2008; Bereiter et al.,
63 2015). A window into older atmospheric CO₂ levels comes from 1 million-year-old blue ice (Higgins
64 et al., 2015) and from a second snapshot from 1.5 Ma (Yan et al., 2019). Most reconstructions of CO₂
65 prior to 800 ka are based on indirect terrestrial and marine proxies. Stomata indices for fossil leaves
66 (Van der Burgh, 1993; Royer, 2001), carbon isotope ratios ($\delta^{13}\text{C}$) of paleosols (Retallak et al., 2009),
67 $\delta^{13}\text{C}$ of alkenones (Pagani et al., 2005; Zhang et al., 2013), B/Ca ratios of surface-dwelling
68 foraminifera (Yu and Hönisch, 2007; Foster, 2008; Tripati et al., 2009, 2011), and boron isotope ratios
69 ($\delta^{11}\text{B}$) of surface-dwelling foraminifera (e.g. Pearson and Palmer., 2000; Hönisch and Hemming,
70 2009; Seki et al., 2010; Bartoli et al., 2011; Foster, 2008, 2012; Badger et al., 2013; Foster and
71 Sexton, 2014; Greenop et al., 2014; Martinez-Botí et al., 2015a; Chalk et al., 2017; Sosdian et al.,
72 2018; Dyez et al., 2018; deLaVega et al., 2020; Greenop et al., 2021; Rae et al., 2021; Raitzsch et al.,
73 2021; Shuttleworth et al., 2021) have been used to estimate atmospheric CO₂.

74 Each of the above proxy methods has sources of systematic errors that we do not attempt to
75 exhaustively document as they have been discussed in-depth elsewhere (e.g., Pagani et al., 2005;
76 Tripati et al., 2011; Guillermic et al., 2020). However, we note that significant developments in the
77 boron-based proxies include improvements to the accuracy and precision of measurements using
78 multi-collector inductively coupled mass spectrometry (MC-ICP-MS) compared to early work with
79 negative thermal ionization mass spectrometry (N-TIMS), where there were large instrumental mass
80 fractionations and challenges with laboratory intercomparison (Foster et al., 2013; Farmer et al., 2016;
81 Aggarwal and You, 2017). There was also the realization that temperature-dependent K_D and B/Ca
82 sensitivities reported from sediment trap, core-top, and downcore studies (Yu and Hönisch, 2007;
83 Foster et al., 2008; Tripati et al., 2009, 2011; Babila et al., 2010; Osborne et al., 2020) differ from
84 inferences from foraminiferal culture experiments (Allen et al., 2011, 2012) and inorganic calcite
85 (Mavromatis et al., 2015) which complicates the use of the B/Ca proxy, although this type of

discrepancy has also been observed with other elemental proxies (e.g., Mg/Ca). Such differences may be due to differences in growth rates (Sadekov et al., 2014), ontogenetic changes, a correlation in the field between temperature and other hydrographic variables that obscure robust statistical determination of parameter relationships, culture conditions resulting in organisms being stressed, and/or other factors.

The marine CO₂ proxy that appears to be subject to the fewest systematic uncertainties, based on our current understanding, is the boron isotopic composition ($\delta^{11}\text{B}$) of planktic foraminifera as measured using MC-ICP-MS and N-TIMS (Hain et al., 2018). This proxy provides constraints on seawater pH, if temperature, salinity, seawater $\delta^{11}\text{B}$, and the appropriate mono-specific calibration between $\delta^{11}\text{B}_{\text{carbonate}}$ and $\delta^{11}\text{B}_{\text{borate}}$ are constrained (Pearson and Palmer, 2000; Foster et al., 2008; Sosdian et al., 2018; Raitzsch et al., 2018; Guillermic et al., 2020). Seawater pH can be used to calculate seawater pCO₂ if there are constraints on a second parameter of the carbonate system (e.g. alkalinity, DIC). Atmospheric pCO₂ can then be constrained if the site being examined is in air-sea CO₂ equilibrium or if the disequilibrium is known and stable through time.

However, there are relatively few studies generating high-precision boron-based records over major climate transitions in the Cenozoic using recent analytical methods and that incorporate our current understanding of the proxy (e.g., Greenop et al., 2014; Martinez-Boti et al., 2015b; Chalk et al., 2017; Dyez et al., 2018; Sosdian et al., 2018; de la Vega et al., 2020; Rae et al., 2021; Raitzsch et al., 2021). Furthermore, of the existing studies using boron-based proxies, an additional uncertainty frequently exists, namely the short time interval of study (e.g., emphasizing on a climate transition) (Martinez-Boti et al., 2015b; Chalk et al., 2017) and whether the study sites remain in air-sea CO₂ equilibrium with the atmosphere (Martinez et al., 2015a). Moreover, although estimation of atmospheric pCO₂ from seawater pH using this proxy is relatively straightforward, reconstructions are still impacted by uncertainties including the lack of robust constraints on a second parameter of the carbonate system, and our limited understanding of secular variations in the $\delta^{11}\text{B}$ of seawater (Tripati et al., 2011; Greenop et al., 2017; Sosdian et al., 2018; Rae et al., 2021).

Therefore, to provide additional constraints on the evolution of atmospheric pCO₂ from the Miocene through Pleistocene, we developed new records from the western tropical Pacific. We use foraminiferal $\delta^{11}\text{B}$ and trace elements in the planktic foraminiferal species *Trilobus sacculifer* and *Globigerinoides ruber* to reconstruct past seawater pH and atmospheric CO₂ at Ocean Drilling Program (ODP) Sites 806 and 807 in the Western Equatorial Pacific (WEP) over the last 16 million years (Myr). The sites are located on the western border of the tropical Pacific Ocean, the largest open ocean region on the globe, and the warmest open ocean region at present.

These two sites have been examined in other boron-based studies (Wara et al., 2003; Tripati et al., 2009, 2011; Shankle et al., 2020), as has the region more broadly (Pearson and Palmer, 2000; Sosdian et al., 2018), because it is understood to be in equilibrium with the atmosphere and have

122 relative stable hydrography. The region experiences equatorial divergence but is not strongly affected
123 by upwelling and has a current estimated annual air-sea CO₂ difference of +28 ppmv (Takahashi et
124 al., 2014). The pre-industrial air-sea CO₂ difference is calculated to be +16 ppm, (GLODAP database
125 corrected from anthropogenic inputs), with a value of 298 ppm, compared to the ice core value of 282
126 ppm at 1.08 ka. This pCO₂ difference is similar to our pCO₂ uncertainty (an average of ~17 ppm (2
127 SD) for the youngest samples). If trade winds were much stronger, and equatorial divergence greater,
128 than this could drive some disequilibrium in the past. However, a few lines of evidence suggest the
129 region was in quasi-equilibrium in the past: 1) zonal temperatures are at a maximum in pre-industrial
130 times and during the Pleistocene, and we are able to reconstruct atmospheric pCO₂ values from the ice
131 cores, 2) temperature proxies indicate the region is relatively stable with respect to temperature
132 compared to other parts of the ocean, and also indicate a weak and stable zonal temperature gradient
133 during the Miocene and Pliocene which would support air-sea stable conditions and air-sea (dis-
134)equilibrium conditions (e.g., Nathan and Leckie, 2009; Zhang et al. 2014; Liu et al., 2019).

135 Thus, this study builds on prior low-resolution reconstructions for these sites (Wara et al.,
136 2003; Tripati et al., 2009, 2011; Shankle et al., 2020), Site 872 in the tropical Pacific (Sosdian et al.,
137 2018), and other published boron isotope work, to provide additional data to constrain past seawater
138 pH and pCO₂ for the WEP using MC-ICP-MS, thereby providing a new perspective on reconstructing
139 past atmospheric CO₂ via marine sediment archives. We explore various constraints on the second
140 carbonate system parameter using a number of different scenarios, following on the systematic work
141 done by Tripati et al. (2009) and (2011) for B/Ca. We interpret these data using recent constraints on
142 seawater $\delta^{11}\text{B}$ (Lemarchand et al., 2000; Raitzsch and Hönnisch, 2013; Greenop et al., 2017). For
143 temperature estimation, we utilize a multi-variable model for Mg/Ca correcting for salinity, pH and
144 seawater Mg/Ca (Gray and Evans, 2019), that builds on prior work with clumped isotopes in planktic
145 foraminifera for Site 806 and other WEP sites demonstrating that for the Last Glacial Maximum to
146 recent times, salinity-corrected Mg/Ca values are needed to yield convergent estimates of mixed-layer
147 temperatures (Tripati et al., 2014).

148

149 **2. Materials and Methods**

150 Below we describe site locations, analytical methods used, and principal figures. The
151 supplemental methods section describes screening for potential contamination, equations used for
152 calculations, and error propagation.

153

154 **2.1 Site locations**

155 Samples are from three ODP holes recovered during Leg 130 in the WEP (Fig. 1, Table 1):
156 Hole 806A (0°19.140'N, 159°21.660'E, 2520.7 m water depth), Hole 806B (0°19.110'N,
157 159°21.660'E, 2519.9 m water depth), and Hole 807A (3°36.420'N, 156°37.500'E, 2803.8 m water

158 depth) (Berger et al., 1993). Sites 806 and 807 are not likely to have experienced major tectonic
159 changes over the last 20 million years.

160

161 **2.2 Preservation**

162 Microfossils in sediments at these sites, as with any sedimentary sequences, have the potential
163 to be influenced by diagenesis. Despite evidence of authigenic carbonate formation, recent modeling
164 work concluded the influence of dissolution and reprecipitation at Sites 806 and 807 was relatively
165 minor (Mitnik et al., 2018). Prior work has also found minimal impacts on the B/Ca ratio of Pliocene
166 foraminifera from Site 806 (White and Ravelo, 2020), and on the Mg/Ca ratio of Miocene *D. altispera*
167 shells at Site 806 (Sosdian et al., 2020). The weight/shell ratio is commonly used to monitor
168 dissolution, and the only published record at Site 806 for the Pliocene does not show a trend
169 consistent with dissolution of *T. sacculifer* (Wara et al., 2005). We do note that while the “coccolith
170 size-free dissolution” index reported in Si and Rosenthal (2019) indicates higher dissolution rates in
171 the Miocene, their records were thought to be biased from changes in foraminifera assemblages as
172 discussed in White and Ravelo (2020).

173 To further assess the potential impact of dissolution in our geochemical data, the weight/shell
174 ratio was examined in our samples. The weight/shell data used to monitor dissolution does not exhibit
175 any trend within the interval studied consistent with dissolution. Absolute weights/shell are increasing
176 in the Miocene, which is not consistent with dissolution influencing the record (Fig. 2E).
177 Additionally, reconstructed pH and pCO₂ values also exhibit reasonable correspondence with the ice
178 core data. Downcore δ¹¹B values from Sites 806 and 807 are similar, despite evidence for higher
179 authigenic carbonate at Site 807 relative to Site 806 (Mitnik et al., 2018). Further, despite different
180 sedimentation rates, our δ¹¹B and Mg/Ca results are consistent between Sites 806 and 807, and with
181 data from Site 872 (Sosdian et al., 2018), which implies that diagenesis is not a primary driver of the
182 reconstructed trends. A comparison of raw data, and derived parameters, is shown in Figs. 2 and 7.

183

184 **2.3 Age models**

185 The age model for Site 806 from 0-1.35 Ma is based on Medina-Elizalde and Lea (2005);
186 calculated ages correspond well with ages from the Lisiecki and Raymo LR04 stack (Fig. 2A). The
187 fourth polynomial regression-based biostratigraphy from Lear et al. (2015) was used for the rest of the
188 record, following other work (Sosdian et al., 2020). Ages for Site 807 are based on published
189 biostratigraphy (Berger et al., 1993) with additional constraints placed by Zhang et al. (2007) for the
190 interval from 0-0.55 Ma. Benthic δ¹⁸O values from Sites 806 and 807 show good correspondence for
191 the last 0.55 Myr, and the low-resolution benthic δ¹⁸O record for Site 806 (Lear et al., 2003; 2015) is
192 consistent with the stack from Lisiecki and Raymo, (2005) for the period studied (Fig. 3).

193

194 **2.4 Species and trace element cleaning**

195 Samples were picked and cleaned to remove clays at UCLA (Los Angeles, CA) and the
196 University of Western Brittany (Plouzané, France). 50-100 foraminifera shells were picked from the
197 300-400µm fraction size for *T. sacculifer* (w/o sacc) and from the 250-300 µm for *G. ruber* (white
198 sensu stricto). Picked foraminifera were gently crushed, clays removed, and checked for coarse-
199 grained silicates. Samples were then cleaned using a full reductive and oxidative cleaning protocol
200 following Barker et al. (2003). A final leach step with 0.001N HCl was done prior dissolution in 1N
201 HCl. Boron purification used a published microdistillation protocol (see Misra et al., 2014b,
202 Guillermic et al., 2020 for more detailed methods).

203

204 **2.5 Chemical purification and geochemical analysis**

205 Chemical separation was performed in a boron-free clean lab at the University of Cambridge
206 (Cambridge, UK). Calcium concentrations were measured on an ICP-AES ®Ultima 2 HORIBA at the
207 Pôle Spectrometrie Océan (PSO), UMR6538 (Plouzané, France). Elemental ratios (e.g. X/Ca ratios)
208 were analyzed on a Thermo Scientific ®Element XR HR-ICP-MS at the PSO, Ifremer (Plouzané,
209 France). Boron isotopic measurements were carried out on a Thermo Scientific ®Neptune+ MC-ICP-
210 MS equipped with 10¹³ Ohm resistor amplifiers (Lloyd et al., 2018) at the University of Cambridge
211 (Cambridge, UK).

212

213 **2.6 Standards**

214 Variations in B isotope ratios are expressed in conventional delta (δ) notation with δ¹¹B values
215 reported against the reference standard NIST SRM 951 (NIST, Gaithersburg, MD, USA):

$$216 \delta^{11}\text{B} (\text{\textperthousand}) = 1000 \times \left(\frac{^{11}\text{B}/^{10}\text{B}_{\text{Sample}}}{^{11}\text{B}/^{10}\text{B}_{\text{NIST SRM 951}}} - 1 \right) \quad \text{eq. 1}$$

217 Multiple analyses of external standards were performed to ensure data quality. For boron
218 isotopic measurements, JC_P-1 (Geological Survey of Japan, Tsukuba, Japan, Gutjahr et al., 2020) was
219 used as a carbonate standard, and NEP, a *Porites sp* coral from University of Western Australia and
220 Australian National University was also used (McCulloch et al., 2014). A boron isotope liquid
221 standard, ERM[®] AE121 (certified δ¹¹B = 19.9 ± 0.6 ‰, SD), was used to monitor reproducibility and
222 drift during each session (Vogl and Rosner, 2012; Foster et al., 2013; Misra et al., 2014b). For trace
223 elements, external reproducibility was determined using the consistency standard Cam-Wuellerstorfi
224 (University of Cambridge) (Misra et al., 2014b).

225

226 **2.7 Figures of Merit**

227 **2.7.1 $\delta^{11}\text{B}$ analyses**

228 Samples measured for boron isotopes typically ranged in concentration from 10 ppb B (~5ng
229 B) to 20 ppb B samples (~10ng B). Sensitivity was 10mV/ppb B (eg. 100mV for 10ppb B) in wet
230 plasma at 50 $\mu\text{l}/\text{min}$ sample aspiration rate. The intensity of ^{11}B for a sample at 10 ppb B was typically
231 104 ± 15 mV (2 SD, typical session) and closely matched the 98 ± 6 mV (2 SD, typical session) of the
232 standard. Procedural boron blanks ranged from 15 pg B to 65 pg B (contributed to less than 1 % of the
233 sample signal). The acid blank during analyses was measured at ≤ 1 mV on ^{11}B (which also is < 1 % of
234 the sample intensity), and no memory effect was seen within and across sessions.

235 External reproducibility was determined by analyzing the international standard JC_P-1
236 (Gutjahr et al., 2020) and a *Porites* sp. coral (NEP). The boron isotopic composition of JC_P-1 was
237 measured at 24.06 ± 0.20 ‰ (2 SD, n=6) within error of published values of 24.37 ± 0.32 ‰, $24.11 \pm$
238 0.43 ‰ and 24.42 ± 0.28 ‰ from Holcomb et al. (2015), Farmer et al. (2016) and Sutton et al. (2018),
239 respectively. Average values are $\delta^{11}\text{B}_{\text{NEP}} = 25.72 \pm 0.79$ ‰ (2 SD, n=31) determined over 13 different
240 analytical sessions, with each number representing a separately processed sample from this study.
241 These results are within error of published values of 26.20 ± 0.88 ‰ (2 SD, n = 27) and 25.80 ± 0.89
242 ‰ (2 SD, n = 6), from Holcomb et al. (2015) and Sutton et al. (2018), respectively. Data are reported
243 in Supplementary Table B.

244

245 **2.7.2 X/Ca analyses**

246 Trace element (TE) analyses were conducted at a Ca concentration of either 10 or 30 ppm.
247 Typical blanks for a 30 ppm Ca session were: $^7\text{Li} < 2$ %, $^{11}\text{B} < 7$ %, $^{25}\text{Mg} < 0.2$ % and $^{43}\text{Ca} < 0.02$ %.
248 Additionally, blanks for a 10 ppm Ca session were: $^7\text{Li} < 2.5$ %, $^{11}\text{B} < 10$ %, $^{25}\text{Mg} < 0.4$ % and $^{43}\text{Ca} <$
249 0.05 %. Analytical uncertainty of a single measurement was calculated from the reproducibility of the
250 CamWuelstorff standard: 0.6 $\mu\text{mol/mol}$ for Li/Ca, 8 $\mu\text{mol/mol}$ for B/Ca and 0.02 mmol/mol for
251 Mg/Ca (2 SD, n=48). Data are reported in Supplementary Table B.

252

253 **2.8 Calculations**

254 Detailed calculations can be found in the supplemental materials. Briefly, Mg/Ca was used to
255 reconstruct sea surface temperature (SST) using the framework from Gray and Evans. (2019)
256 correcting for influences of pH, salinity, and secular variation in seawater Mg/Ca. $\delta^{11}\text{B}_{\text{carbonate}}$ was
257 corrected using an empirical $\delta^{11}\text{B}_{\text{carbonate}}$ -weight/shell ratio relationship. $\delta^{11}\text{B}_{\text{borate}}$ was determined using
258 species dependent sensitivities of $\delta^{11}\text{B}_{\text{carbonate}}$ to $\delta^{11}\text{B}_{\text{borate}}$ (Guillermic et al., 2020). pH was calculated
259 using $\delta^{11}\text{B}_{\text{borate}}$ with different scenarios of secular seawater $\delta^{11}\text{B}$ changes (Lemarchand et al., 2002;
260 Raitzsch and Hönisch, 2013; Greenop et al., 2017). pCO₂ was reconstructed using pH based
261 $\delta^{11}\text{B}_{\text{carbonate}}$ and different scenarios of alkalinity (Tyrell and Zeebe, 2004; Ridgwell and Zeebe, 2005;

262 Caves et al. 2016 and Rae et al. 2021). Further details including equations are provided in the
263 Supplement.

264

265 **3. Results and discussion**

266 **3.1 Geochemical results**

267 Geochemical data used in this study are presented in Figure 2. Mg/Ca data (Fig. 2C) are
268 consistent with previously published Mg/Ca values for Site 806 on *T. sacculifer* (Wara et al., 2005;
269 Tripathi et al., 2009; Nathan and Leckie, 2009). Although the record we generated does not overlap
270 with Site 872, they are 1 Myr apart (15.7 and 16.7 Ma); there is a good correspondence between our
271 Mg/Ca data and the published Mg/Ca record from *T. trilobus* at Site 872 (Sosdian et al., 2018). Mg/Ca
272 from a different species, *D. altispira* (Sosdian et al., 2020), is also plotted with an offset, for
273 comparison.

274 Comparison with Site 872 data that is part of the compilation from Sosdian et al. (2018)
275 shows that their $\delta^{11}\text{B}$ data are in line with our dataset (Figure 2B), and all sites examined in the WEP
276 (Sites 806, 807, and 872) are above the lysocline (Kroenke et al. 1991). The $\delta^{11}\text{B}$ data for *T. sacculifer*
277 exhibit a significant decrease (4.2 ‰) from the Miocene to present. Figure 2B also compares the $\delta^{11}\text{B}$
278 data used in this study with published data from other sites and shows that raw $\delta^{11}\text{B}$ data for the WEP
279 can be lower than values for other regions.

280

281 **3.2 Reproducing pCO₂ from ice cores**

282 We sought to assess if there is evidence for air-sea equilibrium or disequilibrium in the WEP
283 during the large amplitude late Pleistocene glacial/interglacial cycles, in order to validate our
284 approach. We reconstructed pCO₂ for the last 800 kyr (n=16, Fig. 3). For the last 800 kyr,
285 reconstructed pCO₂ values for Sites 806 and 807 are in the range from ice cores (Fig. 3, Petit et al.,
286 1999, Siegenthaler et al., 2005, Lüthi et al., 2008; compilation from Bereiter et al., 2015). The two
287 critical diagnostics we used for method validation are: 1) that the $\delta^{11}\text{B}$ -based reconstruction of pCO₂
288 is consistent with ice core atmospheric CO₂ and 2) the boron-based reconstruction empirically
289 reproduces interglacial-glacial amplitudes from ice cores. Fig. 3B shows that both of these criteria are
290 met despite large scatter. We also created a crossplot comparing these two independent constraints on
291 pCO₂ (Fig. 3C). Two regressions between ice core pCO₂ and boron-based pCO₂ are shown, a simple
292 linear regression (grey line) and a Deming regression that takes into account error in variables (blue
293 line). Bootstrapping was used to calculate uncertainties in the regression models (n=1000, Figure 3C,
294 Table S6). While slopes and intercepts are not statistically different from a 1:1 line, the regressions do
295 not reach a high significance level (p=0.25); boosting the resolution of the record could help provide
296 better constraints for this type of comparison. No significant difference in variability was observed at
297 either site. The age models for the sites are based on comparisons of the benthic $\delta^{18}\text{O}$ records for both

298 Sites 806 and 807 (Fig. 3A, Zhang et al., 2007; Lear et al., 2003; Lear et al., 2015) to the published
299 isotopic stack (Lisiecki and Raymo, 2004).

300 We also note that reconstructed $p\text{CO}_2$ uncertainties (both accuracy and precision) could
301 potentially arise from Mg/Ca-derived estimates of temperature; these uncertainties could be reduced
302 using independent temperature proxies for the WEP such as clumped isotope thermometry (Tripati et
303 al., 2010; 2014), a technique that is not sensitive to the same sources of error as Mg/Ca thermometry,
304 and therefore is an area planned for future work. Other sources of uncertainty that have a larger effect
305 on $p\text{CO}_2$ calculations are the weight/shell correction, while the TA and seawater boron isotope
306 composition have a minor effect over this time interval.

307 Between MIS 7 and 6, our reconstructions exhibit a decrease in temperature (ΔT) of 1.2 °C,
308 an increase in pH (ΔpH) of 0.08 and a decrease in $p\text{CO}_2$ ($\Delta p\text{CO}_2$) of 58 ppm. Between stage 3 and 1,
309 we observed an increase of temperature of 2.0 °C, a decrease of pH of 0.13 and an increase in $p\text{CO}_2$ of
310 76 ppm. We also compare results with recent reconstructions in Figs. S1 and S2 (Sosdian et al., 2018;
311 Rae et al., 2021). These results highlight that we are able to reproduce the range of atmospheric $p\text{CO}_2$
312 in the ice core record, and reproduce the amplitude of changes between transitions, with uncertainties
313 typical for this type of work (Hönisch et al., 2019).

314

315 **3.3 Sea surface temperature in the WEP**

316 Mg/Ca data are consistent at Site 806 (Wara et al., 2005; Tripati et al., 2009, 2011; Nathan
317 and Leckie, 2009) and Site 872 (Sosdian et al., 2018) in the WEP. The Mg/Ca in *T. sacculifer* has to
318 date not shown a pH dependency (Gray and Evans, 2019) but Mg/Ca of *G. ruber* does and was
319 therefore corrected from this effect (see supplemental material). Data for both species were corrected
320 from salinity and seawater Mg/Ca changes. Mg/Ca-temperatures for Site 872 were reconstructed
321 using published data and the same framework we use here and are presented in Figure 4. Recalculated
322 values for Site 872 are from *D. altispera*, with an offset applied relative to *T. sacculifer*, and show
323 similar variations to our record for the MCO-MMCT periods (Sosdian et al., 2020). Temperatures
324 from Tex₈₆ and U^K₃₇ are plotted for comparison but those records are limited to the last 12 and 5
325 Myrs, respectively (Zhang et al., 2014).

326 The Mg/Ca data support high temperatures of 35.2 ± 1.3 °C (2SD, n=11) for the early
327 Miocene until the MMCT, with relatively small (ca. 1°C) change into the MCO, and larger changes
328 out of the MCO. Similarly warm SST for the MCO were reconstructed in the North Atlantic at Site
329 608 from Tex₈₆ (Super et al., 2018). Despite a gap in our compilation from 11.5 to 9.5 Ma, there is a
330 SST decrease of ~6 °C from the MCO to ~7 Ma where temperatures similar to present day values are
331 observed. A decline in temperature during the MMCT is coincident with the timing of a constriction
332 of the Indonesian Seaway, the pre-closure of the trans-equatorial circulation and subsequent formation
333 of a proto-warm pool (Nathan and Leckie, 2009; Sosdian et al., 2020). From 12 to 7 Ma, the Mg/Ca-

334 SST record diverges from Tex₈₆ and U^K₃₇-based reconstructions, with higher temperatures. At the
335 same time, a record for the North Atlantic showed a decrease of ~10 °C from the MCO to ~9 Ma
336 (Super et al., 2018). From 7 Ma to present, the record from multiple proxies – Mg/Ca, Tex₈₆, and
337 U^K₃₇, in the WEP agree.

338

339 **3.4 Scenarios of seawater $\delta^{11}\text{B}$ and alkalinity used for $p\text{CO}_2$ reconstructions**

340 Figures 5 and 6 show the different histories of seawater $\delta^{11}\text{B}$ and alkalinity used in our
341 calculations, respectively. Details of calculations are provided in the Supplemental methods.
342 Following the approach of Tripati et al. (2009, 2014) and recent literature (Sosdian et al., 2018; Rae et
343 al., 2021), we explored multiple scenarios for the evolution of seawater boron geochemistry (Fig. 5)
344 and alkalinity for calculations of $p\text{CO}_2$ (Figs. 6, S1 and S2). During the interval overlapping with the
345 ice core record, we observe that the choice of model used does not make a significant difference in
346 reconstructed values. During earlier time intervals, we see there is a greater divergence, reflecting
347 larger uncertainties in seawater $\delta^{11}\text{B}$ and alkalinity further back in Earth history.

348 Prior to 10 Ma and during the early Pliocene (~4.5 to 3.5 Ma), calculations of $p\text{CO}_2$ diverge
349 from published values largely because of the different assumptions each study has used for past
350 seawater $\delta^{11}\text{B}$ (Fig. 5). However, we find that when the uncertainty in reconstructed pH is fully
351 propagated, the differences in reconstructed pH values calculated using each of the $\delta^{11}\text{B}_{\text{seawater}}$ histories
352 is not significantly different (Fig. 5 and 6; see also Hönisch et al., 2019). In contrast to the results
353 from Greenop et al. (2017), the record from Raitzsch and Hönisch, (2013) exhibits substantial
354 variations on shorter timescales. Such variability is a challenge to reconcile with the Li isotope record
355 of Misra and Froelich, (2012), given that Li has a shorter residence time than boron while having
356 similar sources and sinks. For the remainder of this study, we use the $\delta^{11}\text{B}_{\text{seawater}}$ history from Greenop
357 et al. (2017) because it is in good agreement with seawater $\delta^7\text{Li}$ (Misra and Froelich, 2012). The
358 recent calculations of seawater pH (Sosdian et al., 2018; Rae et al., 2021) agree with values from our
359 study when uncertainties are taken into account (Fig. 5).

360 The four alkalinity models used in this study diverge prior to 9 Ma, with a maximum
361 difference at ~13 Ma that is also reflected in reconstructed $p\text{CO}_2$ values (Fig. 6). However, all four
362 models yield $p\text{CO}_2$ estimates that are within error of each other when the full uncertainty is
363 considered. Uncertainty in the evolution of seawater alkalinity and seawater $\delta^{11}\text{B}$ leads to differences
364 in the absolute values of $p\text{CO}_2$ reconstructed (Fig. S2), and a divergence in $p\text{CO}_2$ values reconstructed
365 that is largest in the Miocene. The two scenarios that produce the highest divergence in values are
366 those calculated using constant alkalinity relative to those calculated using values from McCaves et al.
367 (2016), with a maximum difference at 15.06 Ma of up to 250 ppm CO_2 , and with the latter model
368 producing lower values (Figs. 6B and 6E). Thus, for the MCO, alkalinity is a critical parameter in
369 calculations of absolute $p\text{CO}_2$ values. For the Miocene and earlier intervals, improved constraints on

370 past secular variations of seawater $\delta^{11}\text{B}$ and alkalinity will yield more accurate reconstructions of
371 pCO_2 .

372 For the remainder of this paper, we use the model of Caves et al. (2016) to estimate alkalinity
373 and $\delta^{11}\text{B}_{\text{seawater}}$ determined by Greenop et al. (2017) (e.g. Fig. 6E). We note that two recent syntheses
374 of boron isotope data have been published and compare our results to these findings (Figs. 8 and S2).
375 Sosdian et al. (2018) reports values that are in line with our results in the Miocene but their study does
376 not replicate results from ice cores. Rae et al. (2021) presents reconstructed values that are higher in
377 the Miocene, due to the utilization of different scenarios of seawater $\delta^{11}\text{B}$ and alkalinity compared to
378 this work.

379

380 **3.5 Time intervals**

381 **3.5.1 Miocene**

382 The study of Miocene climate is thought to provide insights into drivers and impacts of global
383 warming and melting of polar ice (Flower and Kennett, 1994). The Miocene epoch (23-5.3 Ma) is
384 characterized by a warm interval, the Miocene Climate Optimum (~17-14.7 Ma - MCO), and an
385 abrupt cooling during the Middle Miocene Climate Transition (~14-13 Ma – MMCT) that led to the
386 expansion of ice on Antarctica and Greenland. Climate modeling supports a role for decreasing CO_2 in
387 this transition (DeConto and Pollard, 2003). However, reconstructions for the Miocene are still
388 relatively limited (Sosdian et al., 2018; Rae et al., 2021; Raitzsch et al., 2021). Boron isotope and
389 alkenone-based pCO_2 reconstructions support higher pCO_2 during the MCO and a decrease over the
390 MMCT (Sosdian et al. 2018; Stoll et al., 2019), consistent with what was previously inferred from
391 B/Ca (Tripati et al., 2009, 2011; Sosdian et al., 2020).

392 We applied the same framework we used for calculations at Sites 806 and 807 to published
393 boron isotope data from Site 872 (Sosdian et al., 2018) in order to extend the WEP record to the early
394 Miocene (Figs. 7, 8). The Miocene data between Sites 806 and 872 do not overlap as both are low in
395 resolution, but do show excellent correspondence in their trends in $\delta^{11}\text{B}$ and reconstructed pH. For
396 example, the closest datapoints in time at the two sites are at 15.6 Ma at Site 806 with a $\delta^{11}\text{B} = 14.47 \pm$
397 0.21 ‰, and at 16.7 Ma at Site 872, with a $\delta^{11}\text{B} = 15.12 \pm 0.25$ ‰. The pH values we reconstruct are
398 within error of published estimates from Site 872 (Sosdian et al. 2018, Figs. 7D and 8D). Collectively,
399 these data suggest that the early Miocene WEP was characterized by a mixed-layer pH of 8.1 ± 0.1 (2
400 SD, $n=4$) between 19.4 and 21.8 Ma, which decreased to reach a minimum during the MCO of 7.7
401 ($\pm_{0.14}^{0.11}$).

402 Given the sensitivity in absolute pCO_2 to assumptions about the second carbonate system
403 parameter, a few scenarios were explored for the combined 806/807/872 reconstructed pH values. For
404 all alkalinity scenarios we used, reconstructed pCO_2 shows an increase from the Early Miocene to the
405 MCO, with the highest values in the MCO. Recalculated pCO_2 for Site 872 between 19.4 and 21.8 Ma

406 is 232 ± 92 ppm (2 SD, n=4), lower but within error of the ones presented in Sosdian et al. (2018) and
407 also within error of a constant alkalinity scenario (Fig. 8D). The main difference between our
408 calculations and published reconstructions occurs between 19.4 and 21.8 Ma, when the same $\delta^{11}\text{B}$
409 data for Site 872 from Sosdian et al. (2018) recalculated in Rae et al. (2021) yield higher pCO₂, with
410 an average value of 591 ± 238 ppm (2 SD, n=4) because of the different assumptions used in their
411 calculations. This difference is important because the assumptions from Rae et al. (2021) would imply
412 a relatively high and stable pCO₂ from the early Miocene to MCO (Fig. S2), which would imply a
413 decoupling between pCO₂ and temperature with no pCO₂ change during an interval of decreasing
414 benthic $\delta^{18}\text{O}$. However, our reconstructed pCO₂ data increase towards the MCO is in line with the
415 observed benthic $\delta^{18}\text{O}$ decrease and $\delta^{13}\text{C}$ increase and suggest a coupling between temperature and
416 pCO₂ over this period. This highlights the critical need for the use of a common set of assumptions for
417 studies. Assumptions may vary between studies depending of the timescales studied, but a common
418 framework is needed. In addition, further constraints on the second carbonate system parameter and
419 on secular changes in seawater $\delta^{11}\text{B}$ will reduce uncertainties in reconstructed pCO₂, with improved
420 precision.

421 The highest pCO₂ values we reconstruct are found during the MCO (Fig. 6E). For the MCO,
422 our estimates are 511 ± 201 ppm (2 SD, n=3, Table 2). The middle Miocene values we reconstruct are
423 in line with previous studies (Greenop et al., 2014; Sosdian et al., 2018). Published $\delta^{11}\text{B}$ -based
424 reconstructions also support higher pCO₂ for the MCO of ~350-400 ppm (Foster et al., 2012) or 300-
425 500 ppm (Greenop et al., 2014) that was recalculated by Sosdian et al. (2018) to be ~470-630 ppm
426 depending on the model of $\delta^{11}\text{B}_{\text{seawater}}$ chosen. During the MCO relative maxima in pCO₂, our data
427 support very warm sea surface temperatures in the WEP (35.6 ± 0.6 °C 2SD, n=3; Fig. 8C), that
428 merits further examination in future studies. In fact, the highest temperatures recorded in our samples
429 occur when there is a minimum in the global composite record of $\delta^{18}\text{O}$ of benthic foraminifera
430 (Zachos et al., 2001, 2008; Tripati and Darby, 2018).

431 At the end of the MMCT, we find evidence for changes in pCO₂ and temperature in the WEP
432 (Fig. 8). From 13.5 to 12.7 Ma, we reconstruct an increase of pH of ~0.21 and a major decrease of
433 pCO₂ of ~215 ppm during an interval highlighted by Flower and Kennett, (1996), who observed
434 changes in $\delta^{18}\text{O}$ indicative of rapid East Antarctic Ice Sheet growth and enhanced organic carbon
435 burial with a maximum $\delta^{13}\text{C}$ reached at ~13.6 Ma (Shevenell et al., 2004; Holbourn et al., 2007). As
436 discussed in section 3.4 the alkalinity model used for the calculations have an important impact during
437 the Miocene which is likely responsible for the different absolute pCO₂ values over the MCO. In
438 comparison, a scenario of constant alkalinity would lead to a pCO₂ during the MCO of 714 ± 313 ppm
439 (2 SD, n=3) and a decrease of ~540 ppm during the MMCT. Both those reconstructions could
440 simulate the large-scale advance and retreat of Antarctic ice with such low pCO₂ values (Gasson et al.,
441 2016). At the same time, we find evidence for a decline in SST of 3.4 °C to minimum values of 33.3

442 °C. The synchronous shifts in the $\delta^{13}\text{C}$ and $\delta^{18}\text{O}$ of benthic foraminifera are consistent with increased
443 carbon burial during colder periods, thus feeding back into decreasing atmospheric CO_2 , and
444 supporting the hypothesis that the drawdown of atmospheric CO_2 can in part, be explained by
445 enhanced export of organic carbon (Flower and Kennett, 1993, 1996). However, given the limited
446 sampling of this study, we are only able to resolve a pCO_2 decrease toward the end of the MMCT
447 (~13.5 Ma). The higher resolution $\delta^{11}\text{B}$ - pCO_2 from Site 1092 for the MMCT (Raitzsch et al. 2021)
448 reports eccentricity-scale pCO_2 variability; the authors reported that low pCO_2 during eccentricity
449 maxima was consistent with an increase in weathering due to strengthened monsoonal circulation,
450 which would increase nutrient delivery and supporting higher productivity that in turn would impact
451 carbon drawdown and burial, in line with modeling from Ma et al. (2011).

452 The resolution of our data during the late Miocene is low, with a data gap from 12.5 to 9.2
453 Ma, and another gap between 6.5 and 5 Ma. We note the pCO_2 peak at ~9 Ma observed by Sosdian et
454 al. (2018) is not seen in our record although this is likely due to the low resolution of our dataset.
455 Between 9.5 and 7.1 Ma we find evidence for a decrease in atmospheric CO_2 of 100 ppm associated
456 with a decrease in temperature of 1.3 °C. pCO_2 estimates derived from alkenones for Site 1088
457 (Tanner et al., 2020) do not show the same trend as boron-based reconstructions from the WEP or
458 other regions (Figure 6), which might be due to other controls on the alkenone proxy (Badger et al.,
459 2019). A recent publication from Raitzsch et al. (2021) reports a $\delta^{11}\text{B}$ reconstruction of pCO_2 that is
460 within error of other $\delta^{11}\text{B}$ isotope data from the Southern Ocean (Sosdian et al., 2018), although not
461 for the same period as Tanner et al. (2020). pCO_2 differences between our reconstruction and that of
462 Sosdian et al. (2018) and Raitzsch et al. (2021) (Fig. 8) likely reflect assumptions made for
463 calculations (of $\delta^{11}\text{B}$, TA) and the specific mono-specific calibrations used for each study, as well as
464 potential geographic differences in air-sea pCO_2 . These differences do not invalidate the boron isotope
465 proxy but illustrate the impact that specific seawater parameters and calibrations can have on
466 reconstructed pCO_2 values, as well as potential inferences of air-sea disequilibrium.

467

468 3.5.2 Pliocene

469 Oxygen isotope data from a global benthic foraminiferal stack show that the Pliocene epoch
470 (5.3-2.6 Ma) was initially characterized by warm conditions followed by the intensification of
471 glaciation that occurred in several steps, including during MIS M2 (3.312-3.264 Ma), followed by the
472 Middle Pliocene Warm Period (Lisiecki and Raymo, 2005). The Middle Pliocene Warm Period
473 (mPWP – 3.29-2.97 Ma) is considered a relevant geological analogue for future climate change given
474 ~3°C warmer global temperatures and sea levels that were ~20 m higher than today (Dutton et al.,
475 2015; Haywood et al., 2016), and is a target for model intercomparison projects, for which accurate
476 paleo-atmospheric pCO_2 estimates are critical (Haywood et al., 2016).

477 We calculate high pCO_2 values of 419 ± 119 ppm (2 SD, n=3, Table 2) between 4.7 to 4.5 Ma

478 during the Early Pliocene warm interval (Figure 9). The pCO₂ data we report provide a higher data
479 density for the Early Pliocene, and exhibit a trend that is in line with the reconstruction from Rae et al.
480 (2021). Our data support values of 530 ± 110 ppm over the mPWP (2 SD, n = 4), higher than
481 previously published data (Figs. 9, S2 and Table 2), although we acknowledge our low data density
482 may not fully sample variability over this period. The similarity between our reconstructed values and
483 those published for Site 871 in the Indian Ocean (Sosdian et al., 2018) suggests that changes in
484 Indonesian through-flow do not induce substantial changes in air-sea exchange in the WEP.

485 The warmth and local pCO₂ maxima of the mPWP (mid-Pliocene Warm Period) was
486 followed by a strong decrease of temperature in upwelling and high latitude regions from 3.3 to 2.7
487 Ma, coincident with glacial intensification in the Northern Hemisphere. This climate transition was
488 hypothesized to be driven by the closure of the Panama seaway the opening of the high latitudes and
489 subsequent modifications of oceanic circulation (Haug and Tiedemann, 1998). However, modeling
490 from Lunt et al. (2008) supports an additional major role for CO₂ in the glaciation. pCO₂ thresholds
491 have been proposed to explain the intensification of Northern Hemisphere Glaciation, with values
492 proposed ranging from 280 ppm (DeConto et al., 2008) to 200 to 400 ppm (Koening et al., 2011).

493 The pCO₂ concentrations that we calculate indicates a reduction to 350 ppm by 2.7 Ma, ~280
494 ppm by 2.6 Ma, and ~210 ppm by 2.4 Ma, in several steps. These results support roughly a halving of
495 CO₂ values when compared to values of ~530 ppm at 3.3 Ma. These values are consistent with the
496 pCO₂ thresholds proposed by both DeConto et al. (2008) and Koening et al. (2011) for the
497 intensification of Northern Hemisphere glaciation and the low atmospheric CO₂ (280 ppmv) scenario
498 from Lunt et al. (2008). Mg/Ca SST decline from 30°C to 26°C, supporting an Earth System
499 sensitivity of ~4°C/doubling of CO₂ over this range, although given uncertainties, higher values of
500 ~6°C/doubling of CO₂ that have recently been proposed (Tierney et al., 2020) can not be excluded.

501 We speculate that associated with Pliocene glacial intensification, at 4.42, 3.45 and 2.67 Ma,
502 it is possible that the declines in CO₂ and ice growth in turn drove substantial changes in pole-to-
503 equator temperature gradients and winds, that in turn may have impacted iron cycling (Watson et al.,
504 2000; Robinson et al., 2005; Martinez-Garcia et al., 2011), stratification (Toggweiler, 1999; Sigman et
505 al., 2010), and other feedbacks that impact the amplitude of glacial/interglacial cycles and have been
506 implicated as factors that could have contributed to Pliocene glacial intensification. Specifically, as
507 the mean climate state of the planet became cooler, and glacial-interglacial cycles became larger in
508 amplitude, enhanced windiness and dust transport and upwelling during glacials (Martinez-Botí et al.,
509 2015b) may have enhanced iron fertilization and subsequent carbon export (Martinez-Garcia et al.,
510 2011). While data resolution is limited, we speculate this could explain why glacial/interglacial
511 amplitudes in WEP pCO₂ values decrease from the mPWP towards the Pleistocene, whereas
512 variations in $\delta^{18}\text{O}$ are increasing – a speculation that could be tested with increased data resolution.

513

514 **3.5.3 Pleistocene**

515 During the Pleistocene (2.58-0.01 Ma), the climate system experienced a transition in
516 glacial/interglacial (G/I) variability from low amplitude, higher frequency and obliquity-dominated
517 oscillations (i.e., ~ 41 kyr) of the late Pliocene to the high amplitude, lower frequency (~100 kyr)
518 cycles of the last 800 kyr. This transition is termed the Middle Pleistocene Transition (1.2-0.8 Ma –
519 MPT). Questions have been raised about the role of atmospheric CO₂ during this transition, including
520 using boron-based proxies (Hönisch et al., 2009; Tripati et al., 2011; Chalk et al., 2017). Previous
521 boron isotope studies for ODP Sites 668 and 999 in the tropical Atlantic Ocean have suggested that a
522 decline in atmospheric CO₂ did occur during glacial periods in the MPT, but not during interglacials
523 (Hönisch et al., 2009; Chalk et al., 2017; Dyez et al., 2018).

524 Our pCO₂ concentrations for Sites 806/807 reported here are in good agreement with those
525 determined from ice cores from the early Pleistocene (Yan et al., 2019, Figs. 9 and 10), and with the
526 boron-derived pCO₂ from a recent compilation (Rae et al., 2021). Results for the MPT are broadly in
527 the range of values reported by Hönisch et al. (2009) and Chalk et al. (2017). Although our data are
528 relatively limited, we note they have greater resolution for the middle and later part of the transition
529 than prior publications that have drawn conclusions about the MPT (Hönisch et al., 2009; Chalk et al.,
530 2017; Dyez et al., 2018) (Fig. 10D) and therefore we explore their implications.

531 Taken alone, or when combined with the published data from Chalk et al. (2017) (that is also
532 based on MC-ICPMS), our results support a possible reduction of both glacial and interglacial pCO₂
533 values. We also find evidence that during the MPT, glacial pCO₂ declined rapidly from 189 ±30 ppm
534 at MIS 36 (Chalk et al., 2017) to reach a minimum of 170 (\pm^{52}_{24}) ppm during MIS 30. We note that
535 pCO₂ concentrations are within error when uncertainty is fully propagated, and then remained
536 relatively stable until the end of the MPT whereas interglacial pCO₂ values decrease gradually to
537 reach post-MPT values.

538 In our record for the last 16 Myr, the lowest pCO₂ is recorded at MIS 30 during the MPT,
539 with values of 164 (\pm^{44}_{35}) ppm, which supports an atmospheric CO₂ threshold that leads to large sheet
540 generation. During this transition, the pCO₂ threshold needed to build sufficiently large ice sheets that
541 were able to survive the critical orbital phase of rising obliquity to ultimately switch to a 100 kyr
542 world, was likely reached at MIS 30, but a higher pCO₂ resolution of the MPT is needed for
543 confirmation. The multiple feedbacks resulting from stable ice sheets (iron
544 fertilization/productivity/changes in albedo/ changes in deep water formation) might have sustained
545 larger mean global ice volumes over the subsequent 800 kyr. An asymmetrical decrease between
546 pCO₂ values during interglacials relative to glacials, with glacials exhibiting the largest change across
547 the MPT, would have led to increased sequestration of carbon during glacials in the 100 kyr world, as
548 discussed by Chalk et al. (2017), with increased glacial dust input and iron fertilization.

549

550 **3.6 Changes in volcanic activity and silicate weathering, and long-term pCO₂**

551 On million-year timescales, atmospheric CO₂ is controlled by its input through mantle
 552 degassing in the form of sub-aerial and sub-aqueous volcanic activity and its removal by chemical
 553 weathering of continental silicate rocks. Over the last 16 Myr, two relative maxima in atmospheric
 554 pCO₂ are observed in our record, one during the MCO (at 15.67 Ma) and a second around the late
 555 Miocene/early Pliocene (beginning at 4.7 and 4.5 Ma) (Fig. 11), though the timing for the latter is not
 556 precise. The strong pCO₂ increase from the early Miocene to MCO occurs when there is increasing
 557 volcanic activity associated with the eruption of the Columbia River Flood Basalts (Hooper et al.,
 558 2002; Foster et al. 2012; Kasbohm and Schoene, 2018), with recent geochronologic evidence published
 559 supporting higher eruption activity between 16.7 and 15.9 Ma (Kasbohm and Schoene, 2018)
 560 reinforcing the idea of an episodic pCO₂ increase during the MCO due to volcanic activity.
 561 Underestimation of net CO₂ outgassing from specific continental flood basalt eruption is possible, as
 562 both sub-aqueous and sub-aerial flood basalts, under right climatic conditions, are prone to enhanced
 563 chemical weathering. For example, the 4-5‰ drop in $\delta^7\text{Li}$ record at the Cretaceous–Paleogene (K-Pg)
 564 boundary (Misra and Froelich, 2012) is attributed to rapid quasi-congruent weathering of Deccan
 565 Traps (Rene et al. 2015) during their eruption. Courtillot and Rene (2003) estimate that about 50% of
 566 emitted CO₂, roughly equivalent to the amount emitted by the eruption of a million cubic kilometers
 567 of Deccan Traps, may be missing due to chemical and physical weathering. Additionally, the early
 568 Eocene (at ~50 Ma) 3-4‰ rise in seawater $\delta^7\text{Li}$ at a time where there is not significant uplift of the
 569 Himalayas (Misra & Froelich, 2012) is also attributed to incongruent weathering of previously
 570 erupted Deccan Trap basalts as the Indian subcontinent moved from arid mid-latitudes to the wet low
 571 latitudes (Kent and Muttoni, 2008). Thus, a significant part of the outgassed CO₂ can be consumed by
 572 chemical weathering of freshly erupted hot basalts (Courtillot et al., 2003). However, the congruency
 573 of chemical weathering of basalts, depending on regional climatic conditions (warm-wet vs. cold-
 574 arid), will determine the shape and position of inflection points in the seawater $\delta^7\text{Li}$ record. The
 575 possible quantification of increased rates of silicate weathering inferred from $\delta^7\text{Li}$ (mentioned below)
 576 can be utilized to determine total eruptive volume (missing + existing) and volatile emissions from the
 577 Columbia River Flood Basalts. At the same time as continental flood basalt emissions, enhanced
 578 seafloor production could also be a second possible source of CO₂; however, we note there is
 579 evidence that the rate of seafloor production has remained virtually invariant over the last 60 million
 580 years (Rowley, 2002; Muller et al. 2016).

581 The second CO₂ peak can possibly be caused either by the observed increase in global
 582 volcanism during the early/middle Pliocene (Kennett and Thunell, 1977; Kroenke et al., 1993), and/or
 583 by a change in silicate weathering regime. Strontium and lithium isotopes ($^{87/86}\text{Sr}$ and $\delta^7\text{Li}$) have been
 584 used as proxy for silicate weathering flux and congruency. Although the strontium isotope record
 585 exhibits a monotonous increase, lithium isotope data (Misra and Froelich, 2012) are more variable

586 with a transition from a period of increasing seawater $\delta^7\text{Li}$ (e.g. non-steady state weathering) to stable
587 seawater $\delta^7\text{Li}$ (e.g., steady state weathering) beginning at roughly 6.8 Ma (Fig. 11).

588 It is interesting to note that the rise in $\delta^7\text{Li}$ (Fig. 11B) from the early Miocene to the MCO is
589 synchronous with the rise in pCO_2 . Before 18.5 Ma, the pCO_2 is relatively stable, $\delta^7\text{Li}$ is increasing,
590 suggesting non-steady state / incongruent nature of continental chemical weathering. From 18.6 to
591 16.7 Ma, the $\delta^7\text{Li}$ record decreases by ~2 ‰, consistent with decreasing weathering rates and an
592 associated increase in pCO_2 . Between 16.7 and 15.9 Ma, when the eruption of the Columbia River
593 Flood Basalts is at a maximum, $\delta^7\text{Li}$ increases, in line with higher weathering rates that could arise
594 from higher atmospheric CO_2 and the presence of fresh basalts. The $\delta^7\text{Li}$ record then decreases again
595 until the end of the MCO at ~14.7 Ma, in line with a decrease in the eruption rate, sustaining high
596 atmospheric CO_2 . A constant increase in $\delta^7\text{Li}$ is then observed, until the early Pliocene, where there is
597 evidence for a shift to a steady-state weathering regime. This increase in $\delta^7\text{Li}$ is also consistent with
598 the decrease in pCO_2 observed until the early Pliocene.
599

600 3.9 Conclusions

601 We developed a reconstruction of atmospheric pCO_2 based on $\delta^{11}\text{B}$ of planktic foraminifera
602 from ODP Sites 806 and 807 located in the Western Equatorial Pacific for the past 16 million years
603 and extended the record to 22 Ma by reprocessing data from Site 872 (Sosdian et al., 2018). We build
604 on past efforts to reconstruct atmospheric pCO_2 using different proxies from this region, including
605 from carbon isotopes in marine organic matter (Rayno et al., 1996) and alkenones (Pagani et al.,
606 2010), as well as foraminiferal B/Ca ratios (Tripati et al., 2009, 2011), all of which have been shown
607 to have a number of complexities and potential sources of systematic error (e.g., Tripati et al., 2011).
608 It also builds on efforts using boron isotopes in other regions using MC-ICP-MS (Seki et al., 2010;
609 Foster et al., 2012, 2014; Greenop et al., 2014; Martinez-Botí et al., 2015b; Stap et al., 2016; Chalk et
610 al., 2017; Dyez et al., 2018; de la Vega et al., 2020), and our recent work constraining fractionation
611 factors and measuring small samples of foraminifera (Guillermic et al., 2020).

612 Our study contributes a new long-term reconstruction of atmospheric pCO_2 for the Neogene
613 derived from boron isotopes from the tropical Pacific Ocean. Although the record is not continuous,
614 with variable resolution, it captures both long-term and short-term variability associated with several
615 key transitions and demonstrates the utility of examining sites in the Western Equatorial Pacific for
616 future higher-resolution studies. Results for Sites 806 and 807 in the Western Equatorial Pacific
617 reproduce the amplitude of late Pleistocene glacial-interglacial cycles in pCO_2 . These observations are
618 consistent with the sites being in equilibrium with the atmosphere, although further work would be
619 useful to explore sources of uncertainty and differences relative to ice core pCO_2 .

620 pCO_2 values increase from the early Miocene to the MCO with estimated MCO pCO_2 values
621 of 511 ± 201 ppm (2 SD, $n=3$). These elevated values are potentially linked to the eruption of the
622 Columbia River Flood Basalts, with values declining into the early Pliocene, including during

623 Pliocene glacial intensification. The changes in pCO₂ we observed are in line with changes in $\delta^7\text{Li}$, a
624 proxy of silicate weathering, and future modeling of multiple proxy records should be insightful.
625 Early Pliocene data for ~4.7-4.5 Ma support high pCO₂ of 419 ± 119 ppm, and elevated values during
626 the mid-Pliocene Warm Period of 530 ± 110 ppm for the time interval ~3.3-3.0 Ma. These data are
627 low in resolution, thereby not fully sampling orbital and millennial scale variability. The higher
628 resolution record for the Pliocene glacial intensification supports a reduction in pCO₂ during several
629 steps, with values at 2.7 Ma of 350 ppm, 2.6 Ma of ~280 ppm, and 2.4 Ma of ~210 ppm. We find
630 support for a larger reduction in glacial pCO₂ during the Mid-Pleistocene Transition compared to
631 interglacial pCO₂, and a minimum in pCO₂ during glacial MIS 30. These findings confirm a role for
632 CO₂ in the transition from a 41 kyr to a 100 kyr world.

633 Higher-resolution boron isotope records from the WEP would allow for further resolution of
634 these changes. Additional constraints on temperature, such as from clumped isotopes (Tripati et al.,
635 2010) in the WEP (Tripati et al., 2014), could allow for uncertainties in pCO₂ estimates from boron
636 isotopes to be reduced and for new constraints on Earth climate sensitivity. Future constraints on the
637 vertical structure of the tropical Pacific (Shankle et al., 2021) during these transitions may also
638 potentially be illuminating.

639

640 **Data availability**

641 All data are available in the supplemental materials. Reconstructed climate parameters and proxy data
642 will be archived at the *NOAA's NCEI World Data Service for Paleoclimatology* on acceptance at
643 <https://www.ncei.noaa.gov/products/paleoclimatology>.

644

645 **Author Contributions**

646 AT developed the project and wrote the proposals that funded the work. All authors contributed to the
647 experimental design. MG performed the measurements with assistance from SM. MG conducted data
648 analysis with input from AT. MG drafted the paper, which was edited by all authors. Interpretation
649 was led by MG and AT, with input from SM and RE.

650

651 **Competing interests**

652 The authors declare that they have no conflict of interest.

653

654 **Acknowledgments**

655 The authors wish to thank the Tripati Lab, including Lea Bonnin and Alexandra Villa, for assistance
656 with picking samples; the IODP core repository for provision of samples; Mervyn Greaves for
657 technical support and use of laboratory space at the University of Cambridge; Yoan Germain,
658 Emmanuel Ponzevera, Céline Liorzou and Oanez Lebeau for technical support and use of laboratory

659 space at IUEM and Ifremer (Plouzané, France). We thank Thomas Chalk, another anonymous
660 reviewer, and Hubertus Fischer for their helpful comments on the manuscript, and Mathis Hain for
661 discussion of this work.

662

663 **Financial support**

664 This research is supported by DOE BES grant no. DE-FG02-13ER16402 to AKT, by the International
665 Research Chair Program that is funded by the French government (LabexMer ANR-10-LABX-19-01)
666 to AKT and RAE, and IAGC student research grant 2017.

667

668 **6. References**

669 Aggarwal, S. K., & You, C. F.: A review on the determination of isotope ratios of boron with mass
670 spectrometry. *Mass Spectrometry Reviews*, 36(4), 499-519, 2017.

671 Allen, K. A. and Hönisch, B.: The planktic foraminiferal B/Ca proxy for seawater carbonate
672 chemistry, A critical evaluation, *Earth Planet. Sci. Lett.*, 345–348, 203–211, 2012.

673 Allen, K. A., Hönisch, B., Eggins, S. M., Yu, J., Spero, H. J., Elderfield, H.: Controls on boron
674 incorporation in cultured tests of the planktic foraminifer *Orbulina universa*. *Earth and Planetary
675 Science Letters*, 309(3-4), 291-301, 2011.

676 Anagnostou, E., John, E. H., Edgar, K. M., Foster, G. L., Ridgwell, A., Inglis, G. N., D. Pancost, R., J.
677 Lunt, D., Pearson, P. N.: Changing atmospheric CO₂ concentration was the primary driver of
678 early Cenozoic climate. *Nature*, 533(7603), 380-384, 2016.

679 Babilia, T., Huang, K. F., Rosenthal, Y., Conte, M. H., & Lin, H. L. Development of B/Ca as a
680 seawater pH proxy using sediment trap time series, abstract, 2010.

681 Badger M. P. S., Chalk T. B., Foster G. L., Bown P. R., Gibbs S. J., Sexton P. F., Schmidt D. N.,
682 Pälike H., Mackensen A. and Pancost R. D.: Insensitivity of alkenone carbon isotopes to
683 atmospheric CO₂ at low to moderate CO₂ levels. *Climate of the Past*, 15(2), 539-554, 2019.

684 Badger M. P. S., Lear C. H., Pancost R. D., Foster G. L., Bailey T. R., Leng M. J. and Abels H. A.:
685 CO₂ drawdown following the middle Miocene expansion of the Antarctic Ice Sheet.
686 *Paleoceanography* 28, 42–53, 2013.

687 Barker S., Greaves M. and Elderfield H.: A study of cleaning procedures used for foraminiferal
688 Mg/Ca paleothermometry. *Geochemistry, Geophys. Geosystems* 4, 1–20, 2003.

689 Bartoli G., Hönisch B. and Zeebe R. E.: Atmospheric CO₂ decline during the Pliocene intensification
690 of Northern Hemisphere glaciations. *Paleoceanography* 26, 1–14, 2011.

691 Berger, W.H., Kroenke, J.W., Mayer, L.A.: Proceedings of the Ocean Drilling Program, Scientific
692 Results, Vol. 130, 1993.

693 Berger, W.H., Kroenke, L., Janecek, T.R., et al., . Proceedings of the Ocean Drilling
694 Program. Initial Reports, p. 130, 1991.

695 Bian, N., & Martin, P. A.: Investigating the fidelity of Mg/Ca and other elemental data from
696 reductively cleaned planktonic foraminifera. *Paleoceanography*, 25(2), 2010.

697 Bolton C. T. and Stoll H. M.: Late Miocene threshold response of marine algae to carbon dioxide
698 limitation. *Nature* 500, 558–562, 2013.

699 Bolton C. T., Hernández-Sánchez M. T., Fuertes M.-Á., González-Lemos S., Abrevaya L., Mendez-
700 Vicente A., Flores J.-A., Probert I., Giosan L., Johnson J. and Stoll H. M. : Decrease in
701 coccolithophore calcification and CO₂ since the middle Miocene. *Nat. Commun.* 7, 10284,
702 2016.

703 Boyer, T.P., J. I. Antonov, O. K. Baranova, C. Coleman, H. E. Garcia, A. Grodsky, D. R. Johnson, R.
704 A. Locarnini, A. V. Mishonov, T.D. O'Brien, C.R. Paver, J.R. Reagan, D. Seidov, I. V. Smolyar,
705 and M. M. Zweng, 2013: World Ocean Database 2013, NOAA Atlas NESDIS 72, S. Levitus,
706 Ed., A. Mishonov, Technical Ed.; Silver Spring, MD, 209 pp.,
707 <http://doi.org/10.7289/V5NZ85MT>, 2013.

708 Brennan, S. T., Lowenstein, T. K., & Cendón, D. I. : The major-ion composition of Cenozoic
 709 seawater: The past 36 million years from fluid inclusions in marine halite. *American Journal of*
 710 *Science*, 313(8), 713-775, 2013.

711 Caves J. K., Jost A. B., Lau K. V. and Maher K.: Cenozoic carbon cycle imbalances and a variable
 712 weathering feedback. *Earth Planet. Sci. Lett.* 450, 152–163, 2016.

713 Chalk T. B., Hain M. P., Foster G. L., Rohling E. J., Sexton P. F., Badger M. P. S., Cherry S. G.,
 714 Hasenfratz A. P., Haug G. H., Jaccard S. L., Martínez-García A., Pálike H., Pancost R. D. and
 715 Wilson P. A.: Causes of ice age intensification across the Mid-Pleistocene Transition. *Proc. Natl.*
 716 *Acad. Sci.*, 201702143, 2017.

717 Coggon R. M., Teagle D. A. H. and Dunkley Jones T. Comment on “What do we know about the
 718 evolution of Mg to Ca ratios in seawater?” by Wally Broecker and Jimin Yu. *Paleoceanography*
 719 26, 2011.

720 DeConto, R. M., & Pollard, D.: Rapid Cenozoic glaciation of Antarctica induced by declining
 721 atmospheric CO₂. *Nature*, 421(6920), 245-249, 2003.

722 DeConto R. M., Pollard D., Wilson P. A., Pálike H., Lear C. H. and Pagani M.: Thresholds for
 723 Cenozoic bipolar glaciation. *Nature* 455, 652–656, 2008.

724 DeFantle M. S. and DePaolo D. J.: Sr isotopes and pore fluid chemistry in carbonate sediment of the
 725 Ontong Java Plateau: Calcite recrystallization rates and evidence for a rapid rise in seawater Mg
 726 over the last 10 million years. *Geochim. Cosmochim. Acta* 70, 3883–3904, 2006.

727 Dekens P. S., Lea D. W., Pak D. K. and Spero H. J.: Core top calibration of Mg/Ca in tropical
 728 foraminifera: Refining paleotemperature estimation. *Geochemistry, Geophys. Geosystems* 3, 1–
 729 29, 2002.

730 Delaney, M. L., Bé, A. W., & Boyle, E. A.: Li, Sr, Mg, and Na in foraminiferal calcite shells from
 731 laboratory culture, sediment traps, and sediment cores. *Geochimica et Cosmochimica Acta*,
 732 49(6), 1327-1341, 1985.

733 de la Vega, E., Chalk, T. B., Wilson, P. A., Bysani, R. P., & Foster, G. L.: Atmospheric CO₂ during
 734 the Mid-Piacenzian Warm Period and the M2 glaciation. *Scientific Reports*, 10(1), 1-8, 2020.

735 Dickson A. G.: Thermodynamics of the Dissociation of Boric Acid in Potassium Chloride Solutions
 736 from 273.15 to 318.15 K. *J. Chem. Eng. Data* 35, 253–257, 1990.

737 Drury, A. J., Lee, G. P., Gray, W. R., Lyle, M., Westerhold, T., Shevenell, A. E., & John, C. M.:
 738 Deciphering the state of the late Miocene to early Pliocene equatorial Pacific. *Paleoceanography*
 739 and paleoclimatology, 33(3), 246-263, 2018.

740 Dyez, K. A., Hönisch, B., & Schmidt, G. A.: Early Pleistocene obliquity-scale pCO₂ variability at~
 741 1.5 million years ago. *Paleoceanography and Paleoclimatology*, 33(11), 1270-1291, 2018.

742 Evans, D. & Müller, W.: Deep time foraminifera Mg/Ca paleothermometry: Nonlinear correction for
 743 secular change in seawater Mg/Ca. *Paleoceanography* 27, PA4205, 2012.

744 Evans, D., Wade, B. S., Henenhan, M., Erez, J., & Müller, W.: Revisiting carbonate chemistry
 745 controls on planktic foraminifera Mg/Ca: implications for sea surface temperature and
 746 hydrology shifts over the Paleocene–Eocene Thermal Maximum and Eocene–Oligocene
 747 transition. *Climate of the Past*, 12(4), 819-835, 2016.

748 Farmer, J. R., Hönisch, B., & Uchikawa, J.: Single laboratory comparison of MC-ICP-MS and N-
 749 TIMS boron isotope analyses in marine carbonates. *Chemical Geology*, 447, 173-182, 2016.

750 Farrell, J.W., Raffi, I., Janecek, T., Murray, D.W., Levitan, M., Dadey, K.A., Emeis, K.C., Lyle, M.,
 751 Flores, J.A., Hovan, S: Late Neogene sedimentation patterns in the eastern Equatorial Pacific
 752 Ocean. In: Pisias, N.G., Mayer, L.A., Janecek, T.R., Palmer-Julson, A., van Andel, T.H. (Eds.),
 753 Proceedings of the Ocean Drilling Program. Scientific Results, vol. 138. ocean Drilling
 754 Program, College Station, TX, pp. 717–756, 1995.

755 Flower, B. P., & Kennett, J. P.: Middle Miocene deepwater paleoceanography in the southwest
 756 Pacific: relations with East Antarctic Ice Sheet development. *Oceanographic Literature Review*,
 757 8(43), 796, 1996.

758 Flower, B. P., & J. P. Kennett: The middle Miocene climatic transition: East Antarctic ice sheet
 759 development, deep ocean circulation and global carbon cycling, *Palaeogeogr. Palaeoclimatol.*
 760 *Palaeoecol.*, 108, 537–555, 1994.

761 Flower, B. P., & Kennett, J. P.: Middle Miocene ocean-climate transition: High-resolution oxygen and
762 carbon isotopic records from Deep Sea Drilling Project Site 588A, southwest Pacific.
763 *Paleoceanography*, 8(6), 811-843, 1993.

764 Ford, H. L., Ravelo, A. C., Dekens, P. S., LaRiviere, J. P., & Wara, M. W.: The evolution of the
765 equatorial thermocline and the early Pliocene El Padre mean state. *Geophysical Research
766 Letters*, 42(12), 4878-4887, 2015.

767 Foster G. L.: Seawater pH, pCO₂and [CO₂-3] variations in the Caribbean Sea over the last 130 kyr: A
768 boron isotope and B/Ca study of planktic foraminifera. *Earth Planet. Sci. Lett.* 271, 254–266,
769 2008.

770 Foster G. L. and Rohling E. J.: Relationship between sea level and climate forcing by CO₂ on
771 geological timescales. *Proc. Natl. Acad. Sci.* 110, 1209–1214, 2013.

772 Foster G. L. and Sexton P. F.: Enhanced carbon dioxide outgassing from the eastern equatorial
773 Atlantic during the last glacial. *Geology* 42, 1003–1006, 2014.

774 Foster, G. L., Hönisch, B., Paris, G., Dwyer, G. S., Rae, J. W., Elliott, T., Gaillardet, J., Hemming, N.
775 G., Louvat, P., Vengosh, A.: Interlaboratory comparison of boron isotope analyses of boric acid,
776 seawater and marine CaCO₃ by MC-ICPMS and NTIMS. *Chemical Geology*, 358, 1-14, 2013.

777 Foster G. L., Lear C. H. and Rae J. W. B.: The evolution of pCO₂, ice volume and climate during the
778 middle Miocene. *Earth Planet. Sci. Lett.* 341–344, 243–254, 2012.

779 Foster G. L., Royer D. L. and Lunt D. J.: Future climate forcing potentially without precedent in the
780 last 420 million years. *Nat. Commun.* 8, 14845. <http://dx.doi.org/10.1038/ncomms14845>, 2017.

781 Gasson E., DeConto R. M., Pollard D. and Levy R. H.: Dynamic Antarctic ice sheet during the early
782 to mid-Miocene. *Proc. Natl. Acad. Sci.* 113, 3459–3464, 2016.

783 Gothmann A. M., Stolarski J., Adkins J. F., Schoene B., Dennis K. J., Schrag D. P., Mazur M. and
784 Bender M. L.: Fossil corals as an archive of secular variations in seawater chemistry since the
785 Mesozoic. *Geochim. Cosmochim. Acta* 160, 188–208, 2015.

786 GraphPad Prism version 7.00 for Windows, GraphPad Software, La Jolla California USA,
787 www.graphpad.com"

788 Gray, W. R., & Evans, D.: Nonthermal influences on Mg/Ca in planktonic foraminifera: a review of
789 culture studies and application to the Last Glacial Maximum. *Paleoceanography and
790 Paleoclimatology*, 34(3), 306-315, 2019.

791 Gray, W. R., Weldeab, S., Lea, D. W., Rosenthal, Y., Gruber, N., Donner, B., & Fischer, G.: The
792 effects of temperature, salinity, and the carbonate system on Mg/Ca in *Globigerinoides ruber*
793 (white): A global sediment trap calibration. *Earth and Planetary Science Letters*, 482, 607-620,
794 2018.

795 Greenop R., Foster G. L., Wilson P. A. and Lear C. H.: Middle Miocene climate instability associated
796 with high-amplitude CO₂ variability. *Paleoceanography* 29, 845–853, 2014.

797 Greenop R., Hain M. P., Sosdian S. M., Oliver K. I. C., Goodwin P., Chalk T. B., Lear C. H., Wilson
798 P. A. and Foster G. L.: A record of Neogene seawater $\delta^{11}\text{B}$ reconstructed from paired $\delta^{11}\text{B}$
799 analyses on benthic and planktic foraminifera. *Clim. Past* 13, 149–170, 2017.

800 Guillermic, M., Misra, S., Eagle, R., Villa, A., Chang, F., Tripati, A.,: Seawater pH reconstruction
801 using boron isotopes in multiple planktonic foraminifera species with different depth habitats
802 and their potential to constrain pH and pCO₂ gradients. *Biogeosciences*, 17(13), 3487-3510,
803 2020.

804 Gutjahr, M., Bordier, L., Douville, E., Farmer, J., Foster, G. L., Hathorne, E. C., J., Foster, G. L.,
805 Hathorne, E., Hönish, B., Lemarchand, D., Louvat, P., McCulloch, M., Noireaux, J., Pallavicini,
806 N., Rodushkin, I., Roux, P., Stewart, J., Thil, F. You, C.F. Sub-permil interlaboratory consistency
807 for solution-based boron isotope analyses on marine carbonates. *Geostandards and
808 Geoanalytical Research*, 2020.

809 Hain, M. P., Foster, G. L., & Chalk, T.: Robust constraints on past CO₂ climate forcing from the
810 boron isotope proxy. *Paleoceanography and Paleoclimatology*, 33(10), 1099-1115, 2018.

811 Hansen, J., Sato, M., & Ruedy, R.: Perception of climate change. *Proceedings of the National
812 Academy of Sciences*, 109(37), 2012.

813 Hansen J., Sato M., Russell G. and Kharecha P.: Climate sensitivity, sea level and atmospheric carbon
814 dioxide. *Philos. Trans. R. Soc. A Math. Phys. Eng. Sci.* 371, 1–38, 2013.

815 Haug, G. H., & Tiedemann, R.: Effect of the formation of the Isthmus of Panama on Atlantic Ocean
816 thermohaline circulation. *Nature*, 393(6686), 673–676, 1998.

817 Haywood, A. M., Dowsett, H. J., & Dolan, A. M.: Integrating geological archives and climate models
818 for the mid-Pliocene warm period. *Nature communications*, 7(1), 1–14, 2016.

819 Hemming N. G. and Hanson G. N.: Boron isotopic composition and concentration in modern marine
820 carbonates. *Geochim. Cosmochim. Acta* 56, 537–543, 1992.

821 Henehan M. J., Foster G. L., Bostock H. C., Greenop R., Marshall B. J. and Wilson P. A.: A new
822 boron isotope-pH calibration for *Orbulina universa*, with implications for understanding and
823 accounting for ‘vital effects.’ *Earth Planet. Sci. Lett.* 454, 282–292, 2016.

824 Henehan M. J., Rae J. W. B., Foster G. L., Erez J., Prentice K. C., Kucera M., Bostock H. C.,
825 Martínez-Botí M. A., Milton J. A., Wilson P. A., Marshall B. J. and Elliott T. (2013) Calibration
826 of the boron isotope proxy in the planktonic foraminifera *Globigerinoides ruber* for use in
827 palaeo-CO₂reconstruction. *Earth Planet. Sci. Lett.* 364, 111–122, 2013.

828 Higgins J. A., Kurbatov A. V, Spaulding N. E., Brook E., Introne D. S., Chimiak L. M., Yan Y.,
829 Mayewski P. A. and Bender M. L.: Atmospheric composition 1 million years ago from blue ice
830 in the Allan Hills, Antarctica. *Proc. Natl. Acad. Sci.* 112, 6887–6891, 2015.

831 Holbourn, A., Kuhnt, W., Schulz, M., Flores, J. A., & Andersen, N.: Orbitally-paced climate
832 evolution during the middle Miocene “Monterey” carbon-isotope excursion. *Earth and Planetary
833 Science Letters*, 261(3-4), 534-550., 2007.

834 Holbourn, A., Kuhnt, W., Schulz, M., Flores, J. A., & Andersen, N.: Orbitally-paced climate
835 evolution during the middle Miocene “Monterey” carbon-isotope excursion. *Earth and Planetary
836 Science Letters*, 261(3-4), 534-550., 2007.

837 Holcomb M., DeCarlo T. M., Schoepf V., Dissard D., Tanaka K. and McCulloch M.: Cleaning and
838 pre-treatment procedures for biogenic and synthetic calcium carbonate powders for
839 determination of elemental and boron isotopic compositions. *Chem. Geol.* 398, 11–21, 2015.

840 Hönisch, B. and Hemming, N. G., Ground-truthing the boron isotope-paleo-pH proxy in planktonic
841 foraminifera shells: Partial dissolution and shell size effects, *Paleoceanography* 19, 1–13, 2004.

842 Hönisch, B., Allen, K. A., Lea, D. W., Spero, H. J., Eggins, S. M., Arbuszewski, J., deMenocal, P.,
843 Rosenthal, Y., D. Russel, a.: Elderfield, H.: The influence of salinity on Mg/Ca in planktic
844 foraminifers—Evidence from cultures, core-top sediments and complementary d 18 O.
845 *Geochimica Et Cosmochimica Acta*, 121, 196–213, 2013.

846 Hönisch, B., Eggins, S. M., Haynes, L. L., Allen, K. A., Holland, K. D., & Lorbacher, K.: Boron
847 Proxies in Paleoceanography and Paleoclimatology. John Wiley & Sons, 2019.

848 Hönisch B., Hemming N. G., Archer D., Siddall M. and McManus J. F.: Atmospheric carbon dioxide
849 concentration across the mid-pleistocene transition. *Science* 324, 1551–1554, 2009.

850 Horita J., Zimmermann H. and Holland H. D.: Chemical evolution of seawater during the
851 Phanerozoic: Implications from the record of marine evaporites. *Geochim. Cosmochim. Acta* 66,
852 3733–3756., 2002.

853 IPCC: Climate Change 2014 - The Physical Science Basis, edited by Intergovernmental Panel on
854 Climate Change, Cambridge University Press, Cambridge., 2014.

855 IPCC: Global Warming of 1.5 °C- edited by Intergovernmental Panel on Climate Change, 2018.

856 Johnstone, H. J., Lee, W., & Schulz, M.: Effect of preservation state of planktonic foraminifera tests
857 on the decrease in Mg/Ca due to reductive cleaning and on sample loss during cleaning.
858 *Chemical Geology*, 420, 23–36, 2016.

859 Kasbohm, J., & Schoene, B.: Rapid eruption of the Columbia River flood basalt and correlation with
860 the mid-Miocene climate optimum. *Science advances*, 4(9), eaat8223, 2018.

861 Kennett, J. P., & Thunell, R. C.: On explosive Cenozoic volcanism and climatic implications. *Science*,
862 196(4295), 1231–1234, 1977.

863 Kisakürek, B., Eisenhauer, A., Böhm, F., Garbe-Schönberg, D., & Erez, J.: Controls on shell Mg/Ca
864 and Sr/Ca in cultured planktonic foraminiferan, *Globigerinoides ruber* (white). *Earth and
865 Planetary Science Letters*, 273(3-4), 260–269, 2008.

866 Klochko K., Kaufman A. J., Yao W., Byrne R. H. and Tossell J. A.: Experimental measurement of
867 boron isotope fractionation in seawater. *Earth Planet. Sci. Lett.* 248, 261–270, 2006.

868 Koenig S. J., DeConto R. M. and Pollard D.: Late Pliocene to Pleistocene sensitivity of the Greenland
869 Ice Sheet in response to external forcing and internal feedbacks. *Clim. Dyn.* 37, 1247–1268,
870 2011.

871 Kroenke, L. W., Berger, W. H., Janecek, T. R. and Shipboard Scientific Party: Proceedings of the
872 Ocean Drilling Program, Initial Reports, Vol. 130, 1991.

873 Lea, D. W.: The 100 000-yr cycle in tropical SST, greenhouse forcing, and climate sensitivity. *Journal
874 of Climate*, 17(11), 2170–2179, 2004.

875 Lee, K., Kim, T. W., Byrne, R. H., Millero, F. J., Feely, R. A., & Liu, Y. M.: The universal ratio of
876 boron to chlorinity for the North Pacific and North Atlantic oceans. *Geochimica et
877 Cosmochimica Acta*, 74(6), 1801–1811, 2010.

878 Lea, D. W., Pak, D. K., & Spero, H. J.: Climate impact of late Quaternary equatorial Pacific sea
879 surface temperature variations. *Science*, 289(5485), 1719–1724, 2000.

880 Lear, C. H., Coxall, H. K., Foster, G. L., Lunt, D. J., Mawbey, E. M., Rosenthal, Y., Sosdian, S. M.,
881 Thomas, E., & Wilson, P. A.: Neogene ice volume and ocean temperatures: Insights from
882 infaunal foraminiferal Mg/Ca paleothermometry. *Paleoceanography*, 30(11), 1437–1454, 2015.

883 Lemarchand D., Gaillardet J., Lewin and Allégre C. J.: The influence of rivers on marine boron
884 isotopes and implications for reconstructing past ocean pH. *Nature* 408, 951–954, 2000.

885 Lisiecki L. E. and Raymo M. E.: A Pliocene-Pleistocene stack of 57 globally distributed benthic $\delta^{18}\text{O}$
886 records. *Paleoceanography* 20, 1–17, 2005.

887 Lloyd, N. S., Sadekov, A. Y. and Misra, S.: Application of 1013ohm Faraday cup current amplifiers
888 for boron isotopic analyses by solution mode and laser ablation multicollector inductively
889 coupled plasma mass spectrometry. *Rapid Commun. Mass Spectrom.*, 32, 9–18, 2018.

890 Lueker, T. J., Dickson, A. G., & Keeling, C. D.: Ocean pCO₂ calculated from dissolved inorganic
891 carbon, alkalinity, and equations for K1 and K2: validation based on laboratory measurements of
892 CO₂ in gas and seawater at equilibrium. *Marine chemistry*, 70(1-3), 105–119, 2000.

893 Lunt D. J., Foster G. L., Haywood A. M. and Stone E. J.: Late Pliocene Greenland glaciation
894 controlled by a decline in atmospheric CO₂ levels. *Nature* 454, 1102–1105, 2008.

895 Lunt, D. J., Haywood, A. M., Schmidt, G. A., Salzmann, U., Valdes, P. J., & Dowsett, H. J.: Earth
896 system sensitivity inferred from Pliocene modelling and data. *Nature Geoscience*, 3(1), 60–64,
897 2010.

898 Lüthi D., Le Floch M., Bereiter B., Blunier T., Barnola J. M., Siegenthaler U., Raynaud D., Jouzel J.,
899 Fischer H., Kawamura K. and Stocker T. F.: High-resolution carbon dioxide concentration
900 record 650,000–800,000 years before present. *Nature* 453, 379–382, 2008.

901 Martínez-Botí, M. A., Marino G., Foster G. L., Ziveri P., Henehan M. J., Rae J. W. B., Mortyn P. G.
902 and Vance D.: Boron isotope evidence for oceanic carbon dioxide leakage during the last
903 deglaciation. *Nature* 518, 219–222, 2015b.

904 Martínez-Garcia, A., Rosell-Melé, A., Jaccard, S. L., Geibert, W., Sigman, D. M., & Haug, G. H.:
905 Southern Ocean dust–climate coupling over the past four million years. *Nature*, 476(7360), 312–
906 315, 2011.

907 Mavromatis, V., Montouillout, V., Noireaux, J., Gaillardet, J. and Schott, J.: Characterization of boron
908 incorporation and speciation in calcite and aragonite from co-precipitation experiments under
909 controlled pH, temperature and precipitation rate, *Geochim. Cosmochim. Acta*, 150, 299–313,
910 2015.

911 McCulloch M. T., Holcomb M., Rankenburg K. and Trotter J. A.: Rapid, high-precision
912 measurements of boron isotopic compositions in marine carbonates. *Rapid Commun. Mass
913 Spectrom.* 28, 2704–2712, 2014.

914 Medina-Elizalde M. and Lea D. W.: The mid-pleistocene transition in the tropical pacific. *Science*
915 310, 1009–1012, 2005.

916 Misra, S. and Froelich, P. N.: Lithium isotope history of cenozoic seawater: Changes in silicate
917 weathering and reverse weathering. *Science* (80-.). 335, 818–823, 2012.

918 Misra, S., Greaves, M., Owen, R., Kerr, J., Elmore, A. C. and Elderfield, H.: Determination of B/Ca
 919 of natural carbonates by HR-ICP-MS. *Geochemistry, Geophys. Geosystems* 15, 1617–1628,
 920 2014a.

921 Misra, S., Owen, R., Kerr, J., Greaves, M. and Elderfield, H.: Determination of $\delta^{11}\text{B}$ by HR-ICP-MS
 922 from mass limited samples: Application to natural carbonates and water samples. *Geochim.
 923 Cosmochim. Acta* 140, 531–552, 2014b.

924 Nathan, S. A., & Leckie, R. M.: *Palaeogeography, Palaeoclimatology, Palaeoecology*, 274(3-4), 140–
 925 159, 2009.

926 Ni Y., Foster G. L., Bailey T., Elliott T., Schmidt D. N., Pearson P., Haley B. and Coath C.: A core
 927 top assessment of proxies for the ocean carbonate system in surface-dwelling foraminifers.
 928 *Paleoceanography* 22, 2007.

929 Nir O., Vengosh A., Harkness J. S., Dwyer G. S. and Lahav O.: Direct measurement of the boron
 930 isotope fractionation factor: Reducing the uncertainty in reconstructing ocean paleo-pH. *Earth
 931 Planet. Sci. Lett.* 414, 1–5, 2015.

932 Nürnberg, D., Bijma, J., & Hemleben, C.: Assessing the reliability of magnesium in foraminiferal
 933 calcite as a proxy for water mass temperatures. *Geochimica et Cosmochimica Acta*, 60(5), 803–
 934 814, 1996.

935 O'Brien C. L., Foster G. L., Martínez-Botí M. A., Abell R., Rae J. W. B. and Pancost R. D.: High sea
 936 surface temperatures in tropical warm pools during the Pliocene. *Nat. Geosci.* 7, 606–611, 2014.

937 Osborne, E. B., Umling, N. E., Bizimis, M., Buckley, W., Sadekov, A., Tappa, E., Marshall, B., R.
 938 Sautter, L., Thunell, R. C.: A Sediment Trap Evaluation of B/Ca as a Carbonate System Proxy in
 939 Asymbiotic and Nondinoflagellate Hosting Planktonic Foraminifera. *Paleoceanography and
 940 Paleoclimatology*, 35(2), 2020.

941 Pagani P., Freeman G., Arthur F., Schuster M., Tiercelin J.-J. and Brunet M.: Late miocene
 942 atmospheric CO₂ concentrations and the expansion of C(4) grasses. *Science* 285, 876–9, 1999.

943 Pagani M., Liu Z., Lariviere J. and Ravelo A. C.: High Earth-system climate sensitivity determined
 944 from Pliocene carbon dioxide concentrations. *Nat. Geosci.* 3, 27–30, 2010.

945 Pagani M., Zachos J. C., Freeman K. H., Tipple B. and Bohaty S.: Atmospheric science: Marked
 946 decline in atmospheric carbon dioxide concentrations during the Paleogene. *Science* 309, 600–
 947 603, 2005.

948 Pearson, P. N., & Palmer, M. R.: Atmospheric carbon dioxide concentrations over the past 60 million
 949 years. *Nature*, 406(6797), 695–699, 2000.

950 Perez, F. F., & Fraga, F.: Association constant of fluoride and hydrogen ions in seawater. *Marine
 951 Chemistry*, 21(2), 161–168, 1987.

952 Petit J. R., Jouzel J., Raynaud D., Barkov N. I., Barnola J. M., Basile I., Bender M., Chappellaz J.,
 953 Davis M., Delaygue G., Delmotte M., Kotiyakov V. M., Legrand M., Lipenkov V. Y., Lorius C.,
 954 Pépin L., Ritz C., Saltzman E. and Stievenard M.: Climate and atmospheric history of the past
 955 420,000 years from the Vostok ice core, Antarctica. *Nature* 399, 429–436, 1999.

956 Pierrot, D., Lewis, E., & Wallace, D. W. R.: MS Excel program developed for CO₂ system
 957 calculations. ORNL/CDIAC-105a. Carbon Dioxide Information Analysis Center, Oak Ridge
 958 National Laboratory, US Department of Energy, Oak Ridge, Tennessee, 10, 2006.

959 Premoli Silva, L., Haggerty, J., Rack, F., et al.: Proceedings of the Ocean Drilling Program, Initial
 960 Reports, Vol. 144, 1993.

961 Rae, J. W., Zhang, Y. G., Liu, X., Foster, G. L., Stoll, H. M., & Whiteford, R. D.: Atmospheric CO₂
 962 over the Past 66 Million Years from Marine Archives. *Annual Review of Earth and Planetary
 963 Sciences*, 49, 2021.

964 Raitzsch M. and Hönnisch B.: Cenozoic boron isotope variations in benthic foraminifers. *Geology* 41,
 965 591–594, 2013.

966 Raitzsch M., Bijma J., Benthien A., Richter K. U., Steinhoefel G. and Kučera M.: Boron isotope-
 967 based seasonal paleo-pH reconstruction for the Southeast Atlantic – A multispecies approach
 968 using habitat preference of planktonic foraminifera. *Earth Planet. Sci. Lett.* 487, 138–150, 2018.

969 Raitzsch, M., Bijma, J., Bickert, T., Schulz, M., Holbourn, A., & Kučera, M.: Atmospheric carbon
 970 dioxide variations across the middle Miocene climate transition. *Climate of the Past*, 17(2), 703–
 971 719, 2021.

972 Ravelo, A. C., Lawrence, K. T., Fedorov, A., & Ford, H. L.: Comment on “A 12-million-year
973 temperature history of the tropical Pacific Ocean”. *Science*, 346(6216), 1467-1467, 2014.

974 Retallack G. J.: Greenhouse crises of the past 300 million years. *Geol. Soc. Am. Bull.* 121, 1441–
975 1455, 2009.

976 Rickaby, R. E. M. and Halloran, P.: Cool La Nina During the Warmth of the Pliocene?, *Science*, 307,
977 1948–1952, 2005.

978 Ridgwell A. and Zeebe R. E.: The role of the global carbonate cycle in the regulation and evolution of
979 the Earth system. *Earth Planet. Sci. Lett.* 234, 299–315, 2005.

980 Royer D. L.: Stomatal density and stomatal index as indicators of paleoatmospheric CO₂
981 concentration. *Rev. Palaeobot. Palynol.* 114, 1–28, 2001.

982 Rowley, D. B.: Rate of plate creation and destruction: 180 Ma to present. *Geological Society of
983 America Bulletin*, 114(8), 927-933, 2002.

984 Russell, A. D., Hönisch, B., Spero, H. J., & Lea, D. W.: Effects of seawater carbonate ion
985 concentration and temperature on shell U, Mg, and Sr in cultured planktonic foraminifera.
986 *Geochimica et Cosmochimica Acta*, 68(21), 4347-4361, 2004.

987 Schmittner, A., Urban, N. M., Shakun, J. D., Mahowald, N. M., Clark, P. U., Bartlein, P. J., Mix A.
988 C., Rosell-Melé, A.: Climate sensitivity estimated from temperature reconstructions of the Last
989 Glacial Maximum. *Science*, 334(6061), 1385-1388, 2011.

990 Seki O., Foster G. L., Schmidt D. N., Mackensen A., Kawamura K. and Pancost R. D.: Alkenone and
991 boron-based Pliocene pCO₂records. *Earth Planet. Sci. Lett.* 292, 201–211, 2010.

992 Shackleton N.J. , Berger A., Peltier W.R.; Trans. R. Soc. Edinb. Earth Sci. 81, 251. Shipboard Leg, O.
993 D. P., Map, O. D. P., & Map, D. S. D.: P. Initial Reports: Volume 130.
994 doi:10.2973/odp.proc.ir.130.108.1991, 1991.

995 Shuttleworth, R., Bostock, H. C., Chalk, T. B., Calvo, E., Jaccard, S. L., Pelejero, C., Martínez-
996 Garcia, A., & Foster, G. L. (2021). Early deglacial CO₂ release from the Sub-Antarctic Atlantic
997 and Pacific oceans. *Earth and planetary science letters*, 554, 116649.

998 Shevenell, A. E., Kennett, J. P., & Lea, D. W.: Middle Miocene southern ocean cooling and Antarctic
999 cryosphere expansion. *Science*, 305(5691), 1766-1770, 2004.

1000 Schlitzer, R., Ocean Data View, <https://odv.awi.de>, 2016.

1001 Siegenthaler, U., Stocker, T. F., Monnin, E., Lüthi, D., Schwander, J., Stauffer, B., Raynaud, D.,
1002 Barnola, JM., Fischer, H., Masson-Delmotte, V., Jouzel, J.: Stable carbon cycle–climate
1003 relationship during the late Pleistocene. *Science*, 310(5752), 1313-1317, 2005.

1004 Sosdian, S. M., Babilia, T. L., Greenop, R., Foster, G. L., & Lear, C. H.: Ocean carbon storage across
1005 the middle Miocene: A new interpretation for the Monterey Event. *Nature communications*,
1006 11(1), 1-11, 2020.

1007 Sosdian, S. M., Greenop R., Hain M. P., Foster G. L., Pearson P. N. and Lear C. H.: Constraining the
1008 evolution of Neogene ocean carbonate chemistry using the boron isotope pH proxy. *Earth
1009 Planet. Sci. Lett.* 498, 362–376, 2018.

1010 Stap L. B., de Boer B., Ziegler M., Bintanja R., Lourens L. J. and van de Wal R. S. W.: CO₂ over the
1011 past 5 million years: Continuous simulation and new δ¹¹B-based proxy data. *Earth Planet. Sci.
1012 Lett.* 439, 1–10, 2016.

1013 Stoll, H. M., Guitian, J., Hernandez-Almeida, I., Mejia, L. M., Phelps, S., Polissar, P., Rosenthal, Y.,
1014 Zhang, H. & Ziveri, P.: Upregulation of phytoplankton carbon concentrating mechanisms during
1015 low CO₂ glacial periods and implications for the phytoplankton pCO₂ proxy. *Quaternary
1016 Science Reviews*, 208, 1-20, 2019.

1017 Super, J. R., Thomas, E., Pagani, M., Huber, M., O’Brien, C., & Hull, P. M.: North Atlantic
1018 temperature and pCO₂ coupling in the early-middle Miocene. *Geology*, 46(6), 519-522, 2018.

1019 Super, J. R., Thomas, E., Pagani, M., Huber, M., O’Brien, C. L., & Hull, P. M.: Miocene Evolution of
1020 North Atlantic Sea Surface Temperature. *Paleoceanography and Paleoclimatology*, 35(5), 2020.

1021 Sutton J. N., Liu Y.-W., Ries J. B., Guillermic M., Ponzevera E. and Eagle R. A.: δ¹¹B as monitor of
1022 calcification site pH in divergent marine calcifying organisms. *Biogeosciences* 15, 1447–1467,
1023 2018.

1024 Takahashi T., Sutherland S. C., Chipman D. W., Goddard J. G. and Ho C.: Climatological
1025 distributions of pH, pCO₂, total CO₂, alkalinity, and CaCO₃saturation in the global surface
1026 ocean, and temporal changes at selected locations. *Mar. Chem.* 164, 95–125, 2014.

1027 Tan, N., Ramstein, G., Dumas, C., Contoux, C., Ladant, J. B., Sepulchre, P., Zhang, Z., De Schepper,
1028 S.: Exploring the MIS M2 glaciation occurring during a warm and high atmospheric CO₂
1029 Pliocene background climate. *Earth and Planetary Science Letters*, 472, 266-276, 2017.

1030 Tanner, T., Hernández-Almeida, I., Drury, A. J., Gutián, J., & Stoll, H.: Decreasing atmospheric CO₂
1031 during the late Miocene Cooling. *Paleoceanography and Paleoclimatology*, e2020PA003925,
1032 2020.

1033 Tierney, J. E., Zhu, J., King, J., Malevich, S. B., Hakim, G. J., & Poulsen, C. J.: Glacial cooling and
1034 climate sensitivity revisited. *Nature*, 584(7822), 569-573, 2020.

1035 Thomas, E.: Descent into the Icehouse. *Geology* 36, 191–192, 2008.

1036 Toggweiler, J. R.: Variation of atmospheric CO₂ by ventilation of the ocean's deepest water.
1037 *Paleoceanography*, 14(5), 571-588, 1999.

1038 Tripati, A., & Darby, D.: Evidence for ephemeral middle Eocene to early Oligocene Greenland glacial
1039 ice and pan-Arctic sea ice. *Nature communications*, 9(1), 1-11, 2018

1040 Tripati A. K., Roberts C. D. and Eagle R. A.: Coupling of CO₂and Ice sheet stability over major
1041 climate transitions of the last 20 million years. *Science* (80). 326, 1394–1397, 2009.

1042 Tripati A. K., Roberts C. D., Eagle R. A. and Li G.: A 20 million year record of planktic foraminiferal
1043 B/Ca ratios: Systematics and uncertainties in pCO₂reconstructions. *Geochim. Cosmochim. Acta*
1044 75, 2582–2610. <http://dx.doi.org/10.1016/j.gca.2011.01.018>, 2011.

1045 Tyrrell, T., & Zeebe, R. E.: History of carbonate ion concentration over the last 100 million years.
1046 *Geochimica et Cosmochimica Acta*, 68(17), 3521-3530, 2004.

1047 Van Der Burgh J., Visscher H., Dilcher D. L. and Kürschner W. M.: Paleoatmospheric signatures in
1048 Neogene fossil leaves. *Science* 260, 1788–1790, 1993.

1049 Vogl J. and Rosner M.: Production and Certification of a Unique Set of Isotope and Delta Reference
1050 Materials for Boron Isotope Determination in Geochemical, Environmental and Industrial
1051 Materials. *Geostand. Geoanalytical Res.* 36, 161–175, 2012.

1052 Wara M. W., Ravelo A. C. and Delaney M. L.: Climate change: Permanent El Niño-like conditions
1053 during the Pliocene warm period. *Science* 309, 758–761, 2005.

1054 Yan, Y., Bender, M. L., Brook, E. J., Clifford, H. M., Kemeny, P. C., Kurbatov, A. V., Mackay, S.,
1055 Mayewski, P.A., Ng, J., Severinghaus, J.P., Higgins, J. A.: Two-million-year-old snapshots of
1056 atmospheric gases from Antarctic ice. *Nature*, 574(7780), 663-666, 2019.

1057 Yu, J., Elderfield, H., Greaves, M., & Day, J.: Preferential dissolution of benthic foraminiferal calcite
1058 during laboratory reductive cleaning. *Geochemistry, Geophysics, Geosystems*, 8(6), 2007a.

1059 Yu J., Elderfield H. and Hönisch B.: B/Ca in planktonic foraminifera as a proxy for surface seawater
1060 pH. *Paleoceanography* 22, 2007.

1061 Zachos J. C., Dickens G. R. and Zeebe R. E.: An early Cenozoic perspective on greenhouse warming
1062 and carbon-cycle dynamics. *Nature* 451, 279–283, 2008.

1063 Zachos, J., Pagani, M., Sloan, L., Thomas, E., & Billups, K.: Trends, rhythms, and aberrations in
1064 global climate 65 Ma to present. *science*, 292(5517), 686-693, 2001.

1065 Zeebe R. E. and Wolf-Gladrow D.: CO₂ in Seawater: Equilibrium, Kinetics, Isotopes Elsevier
1066 Oceanography Series 65, Amsterdam, 2001.

1067 Zhang Y. G., Pagani M., Liu Z., Bohaty S. M. and Deconto R.: A 40-million-year history of
1068 atmospheric CO₂. *Philos. Trans. R. Soc. A Math. Phys. Eng. Sci.* 371, 20130096–20130096,
1069 2013.

1070 Zhang, Y. G., Pagani, M., & Liu, Z.: A 12-million-year temperature history of the tropical Pacific
1071 Ocean. *Science*, 344(6179), 84-87, 2014.

1072 Zhang, J., Wang, P., Li, Q., Cheng, X., Jin, H., & Zhang, S.: Western equatorial Pacific productivity
1073 and carbonate dissolution over the last 550 kyr: Foraminiferal and nannofossil evidence from
1074 ODP Hole 807A. *Marine Micropaleontology*, 64(3-4), 121-140, 2007.

1075 **Figure captions**

1076 **Figure 1:** Modern hydrography of sites. **A.** Map of air-sea $\Delta p\text{CO}_2$ (ppm, data from Takahashi
1077 et al. (2014) and plotted using Ocean Data View from Schlitzer, (2016) showing the location of ODP
1078 Sites 806 and 807 (black circles) and Site 872 (black square, Premoli et al., 1993). Depth profiles are
1079 for preindustrial parameters, **B.** pH calculated from GLODAP database and corrected for
1080 anthropogenic inputs, **C.** Boron isotopic composition of borate ion ($\delta^{11}\text{B}_{\text{borate}}$) with associated
1081 propagated uncertainties.

1082 **Figure 2:** Foraminiferal data for Miocene to recent times. **A.** Benthic foraminiferal $\delta^{18}\text{O}$ data (blue
1083 line – stack from Lisiecki and Raymo, 2005; black line – compilation from Zachos et al., 2008). **B.**
1084 $\delta^{11}\text{B}$ of *T. sacculifer* (blue circles) and *G. ruber* (blue triangles) at Sites 806 (light blue), 807 (dark
1085 blue), Grey filled square represent data from Site 872 located in the WEP (Sosdian et al., 2018). Open
1086 symbols are $\delta^{11}\text{B}$ data from published studies (Hönisch and Hemming, 2009; Seki et al., 2010; Foster
1087 et al., 2012; Greenop et al., 2014; Martinez-Boti et al., 2015a; Chalk et al., 2017; Dyez et al., 2018;
1088 Sosdian et al., 2018; de la Vega et al., 2020; Raitzsch et al., 2021), grey open symbols are *T.*
1089 *sacculifer*, brown open symbols are for *G. ruber*. **C.** Mg/Ca ratios of *T. sacculifer* and *G. ruber* at
1090 Sites 806, 807 and fourth-order polynomial regression from Sosdian et al. (2020) representing secular
1091 variations of Mg/Ca_{sw} (blue dotted line). **E.** Calculated weight per shell for *T. sacculifer* and *G. ruber*.
1092 For Panels B-D: Circles = *T. sacculifer*, Triangles = *G. ruber*.

1093 **Figure 3:** **A.** Reconstruction of surface pCO_2 (ppm) for the past 0.8 Myr from *T. sacculifer* at ODP
1094 Sites 806 and 807 (blue symbols) using boron-based pH calculated from $\delta^{11}\text{B}_{\text{seawater}}$ (Greenop et al.,
1095 2017) and alkalinity from Caves et al. (2016). Planktonic foraminiferal $\delta^{18}\text{O}$ at site 806 with isotope
1096 stages labeled (black line – Medina-Elizalde and Lea, 2005) and benthic foraminiferal $\delta^{18}\text{O}$ stack
1097 (grey line - Lisiecki and Raymo, 2005), benthic $\delta^{18}\text{O}$ at Site 806 (dark red line) from Lear et al. (2003,
1098 2015). **B.** pCO_2 values calculated from boron isotopes (colored symbols - this study) with data from
1099 the literature (open gray triangles – compilation B are data recalculated in Rae et al., 2021) and ice
1100 core pCO_2 (black line – Petit et al., 1999, Lüthi et al., 2008, Bereiter et al., 2015). **C.** Cross plot for the
1101 last 0.8 Myr of pCO_2 $\delta^{11}\text{B}$ from this study and pCO_2 ice core (from ice core compilation, Bereiter et al.,
1102 2015), grey line is a simple linear regression ($p = 0.25$, $R^2=0.09$), blue line is a Deming regression
1103 taking both x and y uncertainties into account ($p = 0.25$). Details of the regression parameters are in
1104 Table S6. Ice core CO_2 error was calculated based on 2 SD of reported values, and ± 1 ky for the age
1105 of sediment samples. Boron-based pCO_2 error is calculated based on error propagation described by
1106 eq. S17. Data compiled are from: Foster et al., 2008; Hönisch and Hemming, 2009; Seki et al., 2010;
1107 Foster et al., 2012; Badger et al., 2013; Greenop et al., 2014; Martinez-Boti et al., 2015a; Chalk et al.,
1108 2017; Dyez et al., 2018; Sosdian et al., 2018; Greenop et al., 2019; de la Vega et al., 2020.

1109 **Figure 4:** Compilation of temperatures from Site 806 in the WEP. Mg/Ca based temperatures were
1110 derived using the same framework (see supplemental information). Blue filled symbols are from Sites
1111 806 and 807 with blue circles for *T. sacculifer* and triangles for *G. ruber*; filled gray squares are data
1112 from Site 872 (Sosdian et al., 2018). Open symbols are SST derived from Mg/Ca at Site 806 (Wara et
1113 al., 2005; Tripathi et al., 2009; Nathan and Leckie, 2009). Tex₈₆ and U₃₇^K are also plotted for
1114 comparison (Zhang et al., 2014). Orange open circles are SST data calculated with our framework
1115 from the species *D. altispera* at ODP Site 806 (Sosdian et al., 2020) with an offset of +8°C. Blue line
1116 is a smooth line (Lowess) going through the data.

1117
1118 **Figure 5:** Different models for the evolution of the boron geochemistry explored as part of this work.
1119 Due to the 1 % uncertainty propagated for $\delta^{11}\text{B}_{\text{seawater}}$, all scenarios yield reconstructed seawater pH
1120 values that are within error of each other. Propagated uncertainties were calculated using eq. S14 (see
1121 Supplement). **A.** Different models for $\delta^{11}\text{B}_{\text{seawater}}$ used for the reconstruction of pCO_2 in this study
1122 (blue – Lemarchand et al., 2000; green – Greenop et al., 2017; red – Raitzsch and Hönisch, 2013). **B.**
1123 Reconstructed pH based on our measured $\delta^{11}\text{B}_{\text{carbonate}}$ values using different models for $\delta^{11}\text{B}_{\text{seawater}}$
1124 (blue – Lemarchand et al., 2000; green – Greenop et al., 2017; red – Raitzsch and Hönisch, 2013),

compilations of pH from Sosdian et al. (2018) (compilation A - open squares) and Rae et al. (2021) (compilation B - open triangles) are also shown for comparison. Data for compilation A are from: Hönisch and Hemming, 2009; Seki et al., 2010; Foster et al., 2012; Badger et al., 2013; Greenop et al., 2014; Martinez-Botí et al., 2015a; Chalk et al., 2017; Sosdian et al., 2018. Data for compilation B are from: Foster et al., 2008; Hönisch and Hemming, 2009; Seki et al., 2010; Foster et al., 2012; Badger et al., 2013; Greenop et al., 2014; Martinez-Botí et al., 2015a; Chalk et al., 2017; Dyez et al., 2018; Sosdian et al., 2018; Greenop et al., 2019; de la Vega et al., 2020.

Figure 6: Different models for the evolution of a second carbonate (e.g. alkalinity) system parameter explored as part of this work. The propagated uncertainties were calculated using eq. S16 (see Supplement). **A.** Different models for alkalinity used for the reconstruction of $p\text{CO}_2$ in this study (brown – constant alkalinity of 2330 $\mu\text{mol/kg}$, blue - Ridgwell and Zeebe, 2005; green - Tyrell and Zeebe, 2004; violet - Caves et al., 2016. Colored symbols are reconstructed $p\text{CO}_2$ based on our measured $\delta^{11}\text{B}_{\text{carbonate}}$ values , alkalinity scenario and $\delta^{11}\text{B}_{\text{seawater}}$ from Greenop et al., 2017; open squares (compilation A) are $p\text{CO}_2$ compilation from Sosdian et al. (2018), open triangles (compilation B) are from the compilation by Rae et al. (2021), black symbols are from site 872. **B.** Reconstructed $p\text{CO}_2$ using constant alkalinity of 2330 $\mu\text{mol/kg}$ and $\delta^{11}\text{B}_{\text{seawater}}$ from Greenop et al. (2017). **C.** Reconstructed $p\text{CO}_2$ using the constant alkalinity scenario from Ridgwell and Zeebe, (2005) and $\delta^{11}\text{B}_{\text{seawater}}$ from Greenop et al. (2017). **D.** Reconstructed $p\text{CO}_2$ using constant alkalinity scenario from Tyrell and Zeebe, (2004) and $\delta^{11}\text{B}_{\text{seawater}}$ from Greenop et al. (2017). **E.** Reconstructed $p\text{CO}_2$ using constant alkalinity scenario from Caves et al., (2016) and $\delta^{11}\text{B}_{\text{seawater}}$ from Greenop et al. (2017). In black are published estimates from ice core data (circles - Yan et al., 2019). Compilations of $p\text{CO}_2$ from Sosdian et al. (2018) (compilation A - open squares) and Rae et al. (2021) (compilation B - open triangles) are also shown for comparison. Data for compilation A are from: Hönisch and Hemming, 2009; Seki et al., 2010; Foster et al., 2012; Badger et al., 2013; Greenop et al., 2014; Martinez-Botí et al., 2015a; Chalk et al., 2017; Sosdian et al., 2018. Data for compilation B are from: Foster et al., 2008; Hönisch and Hemming, 2009; Seki et al., 2010; Foster et al., 2012; Badger et al., 2013; Greenop et al., 2014; Martinez-Botí et al., 2015a; Chalk et al., 2017; Dyez et al., 2018; Sosdian et al., 2018; Greenop et al., 2019; de la Vega et al., 2020. Stars indicate $p\text{CO}_2$ values reconstructed from alkenones by Tanner et al. (2020) (simulation 6) at Site 1088 in the Southern Ocean.

Figure 7: Proxy data for the past 22 million years in the Western Equatorial Pacific compared to benthic oxygen isotope data. **A.** Benthic $\delta^{18}\text{O}$ (blue line – stack from Lisiecki and Raymo, 2005; black line – compilation from Zachos et al., 2008). **B.** Benthic $\delta^{13}\text{C}$ (black line – compilation from Zachos et al., 2008). **C to E**, color indicates the site (filled light blue=806, filled dark blue=807), symbols represent the species (circle=*T. sacculifer* and triangle=*G. ruber*), filled grey squares are recalculated data based on Sosdian et al. (2018) at site 872. **C.** SST reconstructed at ODP Sites 806 and 807 using Mg/Ca ratios (see supplemental information for reconstruction details), open symbols are reconstructed temperatures based on literature Mg/Ca at site 806 (see text or Fig. 4). **D.** Seawater pH reconstructed from $\delta^{11}\text{B}$ of *T. sacculifer* and *G. ruber* using $\delta^{11}\text{B}_{\text{seawater}}$ from Greenop et al. (2017) (refer to text and supplement for calculations, this study), open squares (compilation A) represent data from the CO_2 compilation of Sosdian et al. (2018) and open triangles (compilation B) are compilation data from Rae et al. (2021). **E.** Reconstructed $p\text{CO}_2$ (ppm) using boron-based pH and alkalinity from Caves et al. (2016), data presented are from this study. Propagated uncertainties are given by eq. S17 for the dark blue envelope, while the light blue envelope are the uncertainties calculated based on eq. S16 (taking into account uncertainty in $\delta^{11}\text{B}_{\text{seawater}}$). Crosses are original $p\text{CO}_2$ values calculated in Sosdian et al. (2018) at Site 872; asterisks are recalculated $p\text{CO}_2$ values at Site 872 by Rae et al. (2021).

Figure 8: Proxy data from 22 to 6 million years, including the Middle Miocene Climate Transition (MMCT) and Miocene Climate Optimum (MCO), in the Western Equatorial Pacific compared to benthic oxygen isotope data. **A.** Benthic $\delta^{18}\text{O}$ (black line – compilation from Zachos et al., 2008). **B.** Benthic $\delta^{13}\text{C}$ (black line – compilation from Zachos et al., 2008). **C and D**, color indicates the site

(filled light blue=806, filled dark blue=807), symbols represent the species (circle=*T. sacculifer* and triangle=*G. ruber*), filled grey squares are recalculated data based on Sosdian et al. (2018) at site 872. **C.** SST reconstructed at ODP Sites 806 and 807 using Mg/Ca ratios (see supplemental informations for reconstruction details), open symbols are reconstructed temperatures based on literature Mg/Ca at site 806 (see text or Fig. 4). **D.** Reconstructed pCO₂ (ppm) from this study (blue symbols) using boron-based pH and alkalinity from Caves et al. (2016). Propagated uncertainties are given by eq. S17 for the dark blue envelope, while the light blue envelope reflects the uncertainties calculated based on eq. S16 (taking into account uncertainty on $\delta^{11}\text{B}_{\text{seawater}}$). Orange datapoints and envelope are calculated pCO₂ values and associated uncertainty from our study using our framework and a constant alkalinity scenario. Open squares (compilation A) are compilation data from Sosdian et al. (2018), open triangles are data from Raitzsch et al. (2021) at Site 1092. Crosses are original pCO₂ calculated in Sosdian et al. (2018) at Site 872; asterisks are recalculated pCO₂ at Site 872 by Rae et al. (2021); dark red triangles are from Site 1092 (Raitzsch et al., 2021). Data for compilation A are from: Hönisch and Hemming, 2009; Seki et al., 2010; Foster et al., 2012; Badger et al., 2013; Greenop et al., 2014; Martinez-Botí et al., 2015a; Chalk et al., 2017; Sosdian et al., 2018. Data for compilation B are from: Foster et al., 2008; Hönisch and Hemming, 2009; Seki et al., 2010; Foster et al., 2012; Badger et al., 2013; Greenop et al., 2014; Martinez-Botí et al., 2015a; Chalk et al., 2017; Dyez et al., 2018; Sosdian et al., 2018; Greenop et al., 2019; de la Vega et al., 2020.

Figure 9: Proxy data from 7 to 1 million years, including the Warm Pliocene Transition (WPT), in the Western Equatorial Pacific compared to benthic oxygen isotope data. **A.** Benthic $\delta^{18}\text{O}$ (black line – compilation from Zachos et al., 2008). **B.** Benthic $\delta^{13}\text{C}$ (black line – compilation from Zachos et al., 2008). **C and D**, color indicates the site (filled light blue=806, filled dark blue=807), symbols represent the species (circle=*T. sacculifer* and triangle=*G. ruber*), filled grey squares are recalculated data based on Sosdian et al. (2018) at ODP Site 872. **C.** SST reconstructed at ODP Sites 806 and 807 using Mg/Ca ratios (see supplemental informations for reconstruction details), open symbols are reconstructed temperatures based on literature Mg/Ca at site 806 (see text or Fig. 4). **D.** Reconstructed pCO₂ (ppm) from this study (blue symbols) using boron-based pH and alkalinity from Caves et al. (2016). Propagated uncertainties are given by eq. S17 for the dark blue envelope, while the light blue envelope reflects the uncertainties calculated based on eq. S16 (taking into account uncertainty on $\delta^{11}\text{B}_{\text{seawater}}$). Open squares (compilation A) are pCO₂ compilation from Sosdian et al. (2018), open triangles (compilation B) are from the compilation by Rae et al. (2021). Data for compilation A are from: Hönisch and Hemming, 2009; Seki et al., 2010; Foster et al., 2012; Badger et al., 2013; Greenop et al., 2014; Martinez-Botí et al., 2015a; Chalk et al., 2017; Sosdian et al., 2018. Data for compilation B are from: Foster et al., 2008; Hönisch and Hemming, 2009; Seki et al., 2010; Foster et al., 2012; Badger et al., 2013; Greenop et al., 2014; Martinez-Botí et al., 2015a; Chalk et al., 2017; Dyez et al., 2018; Sosdian et al., 2018; Greenop et al., 2019; de la Vega et al., 2020. In black are published estimates from ice core data (circles - Yan et al., 2019).

Figure 10: Proxy data from 1.5 to 0.5 million years, including the Middle Pleistocene Transition (MPT), in the Western Equatorial Pacific compared to benthic oxygen isotope data. **A.** Benthic $\delta^{18}\text{O}$ (blue line – stack from Lisiecki and Raymo, 2005). **B.** Benthic $\delta^{13}\text{C}$ (black line – compilation from Zachos et al., 2008). **C and D** color indicates the site (filled light blue=806, filled dark blue=807), symbols represent the species (circle=*T. sacculifer* and triangle=*G. ruber*), filled grey squares (compilation A) are recalculated data based on Sosdian et al. (2018) at site 872. **C.** SST reconstructed at ODP Sites 806 and 807 using Mg/Ca ratios (see supplemental informations for reconstruction details), open symbols are reconstructed temperatures based on literature Mg/Ca at site 806 (see text or Fig. 4). **D.** Reconstructed pCO₂ (ppm) from this study (blue symbols) using boron-based pH and alkalinity from Caves et al. (2016). Propagated uncertainties are given by eq. S17. In black are published estimates from ice core data (line – Bereiter et al., 2015; black circles - Yan et al., 2019). Open triangles (compilation B) are from the compilation by Rae et al. (2021). Data for compilation B are from: Foster et al., 2008; Hönisch and Hemming, 2009; Seki et al., 2010; Foster et al., 2012; Badger et al., 2013; Greenop et al., 2014; Martinez-Botí et al., 2015a; Chalk et al., 2017; Dyez et al., 2018; Sosdian et al., 2018; Greenop et al., 2019; de la Vega et al., 2020.

1229
1230
1231
1232
1233
1234
1235
1236
1237
1238
1239
1240
1241
1242
1243
1244
1245
1246
1247
1248
1249
1250
1251
1252
1253
1254

Figure 11: Proxy data from 1.5 to 0.5 million years, including the Middle Pleistocene Transition (MPT), in the Western Equatorial Pacific compared to benthic oxygen isotope composites. **A.** Benthic $\delta^{18}\text{O}$ (blue line – compilation from Lisiecki and Raymo, 2005, black line – compilation from Zachos et al. 2008). **B.** Records from Lithium isotopes ($\delta^7\text{Li}$, orange, Misra and Froelich, 2012) and Strontium isotopes ($^{87/86}\text{Sr}$, grey, Hodell et al., 1991, Farrel et al., 1995, Martin et al., 1999, Martin et al., 2004), both proxies for silicate weathering. Orange arrows represent the different weathering regimes as indicated by the $\delta^7\text{Li}$, black crosses indicates when changes in weathering regime occur. **C.** Reconstructed pCO_2 (ppm) using boron-based pH and alkalinity from Caves et al. (2016), color indicates the site (filled light blue=806, filled dark blue=807), symbols represent the species (circle=*T. sacculifer* and triangle=*G. ruber*), filled grey squares (compilation A) are recalculated data based on Sosdian et al. (2018) at site 872. Data for compilation A are from: Hönisch and Hemming, 2009; Seki et al., 2010; Foster et al., 2012; Badger et al., 2013; Greenop et al., 2014; Martinez-Botí et al., 2015a; Chalk et al., 2017; Sosdian et al., 2018. Propagated uncertainties are given by eq. S17 for the dark blue envelope, while the light blue envelope are the uncertainties calculated based on eq. S16 (taking into account uncertainty on $\delta^{11}\text{B}_{\text{seawater}}$). Also shown is the timing of major events. The rose band and dark rose band indicate the eruption of the Columbia River flood basalts (Hooper et al., 2002) and time of maximum eruption (Kasbohm and Schoene, 2018), respectively.

Table 1: Core information.

Cruise	Leg	Hole	N (°)	E (°)	Depth (m)
ODP	130	807	3.61	156.62	2804
ODP	130	806	0.32	159.37	2520

Table 2: Comparison of reconstructed pCO₂ values for key intervals in the last 16 Myr.

Mid-Pleistocene transition (1.2-0.8 Ma)		MIS (IG) pCO₂ (ppm) Reference		pCO₂ amplitude IG-G (ppm)	
MIS (G)	pCO₂ (ppm)	Reference	MIS (IG) pCO₂ (ppm)	Reference	
20	179	This study	21	254	This study
22	187	This study	23	230	This study
24	nd		25	298	This study
26	nd		27	nd	
28	174	This study	29	nd	
30	170	This study	31	295	Hönisch et al., 2009 (N-TIMS)
32	218	Chalk et al., 2017	33	323	Chalk et al., 2017
34	197	Chalk et al., 2017	35	315	Chalk et al., 2017
36	189	Chalk et al., 2017	37	295	This study, Chalk et al., 2017
			39	306	This study
Middle Pliocene Warm Period (3.29-2.97 Ma) <th data-kind="ghost"></th> <th data-cs="4" data-kind="parent"></th> <th data-kind="ghost"></th> <th data-kind="ghost"></th> <th data-kind="ghost"></th>					
pCO₂ (ppm)	Reference				
530 ± 110	This study (2 SD, n=4)				
320 ± 130	Martinez-Botí et al., 2015b (2 SD, n=8)				
360 ± 85	de la Vega et al., 2020 (2 SD, n=59)				
Early Pliocene Warm Period (4.7-4.5 Ma) <th data-kind="ghost"></th> <th data-cs="4" data-kind="parent"></th> <th data-kind="ghost"></th> <th data-kind="ghost"></th> <th data-kind="ghost"></th>					
pCO₂ (ppm)	Reference				
419 ± 119	This study (2 SD, n=3)				
Miocene Climate Optimum (17-14 Ma) <th data-kind="ghost"></th> <th data-cs="4" data-kind="parent"></th> <th data-kind="ghost"></th> <th data-kind="ghost"></th> <th data-kind="ghost"></th>					
pCO₂ (ppm)	Reference				
511 ± 201	This study (2 SD, n=3)				
350-400	Foster et al., 2012				
300-500	Greenop et al., 2014				
470-630	Sosdian et al., 2018				
687 ± 421	Rae et al., 2021 (2 SD, n=58)				

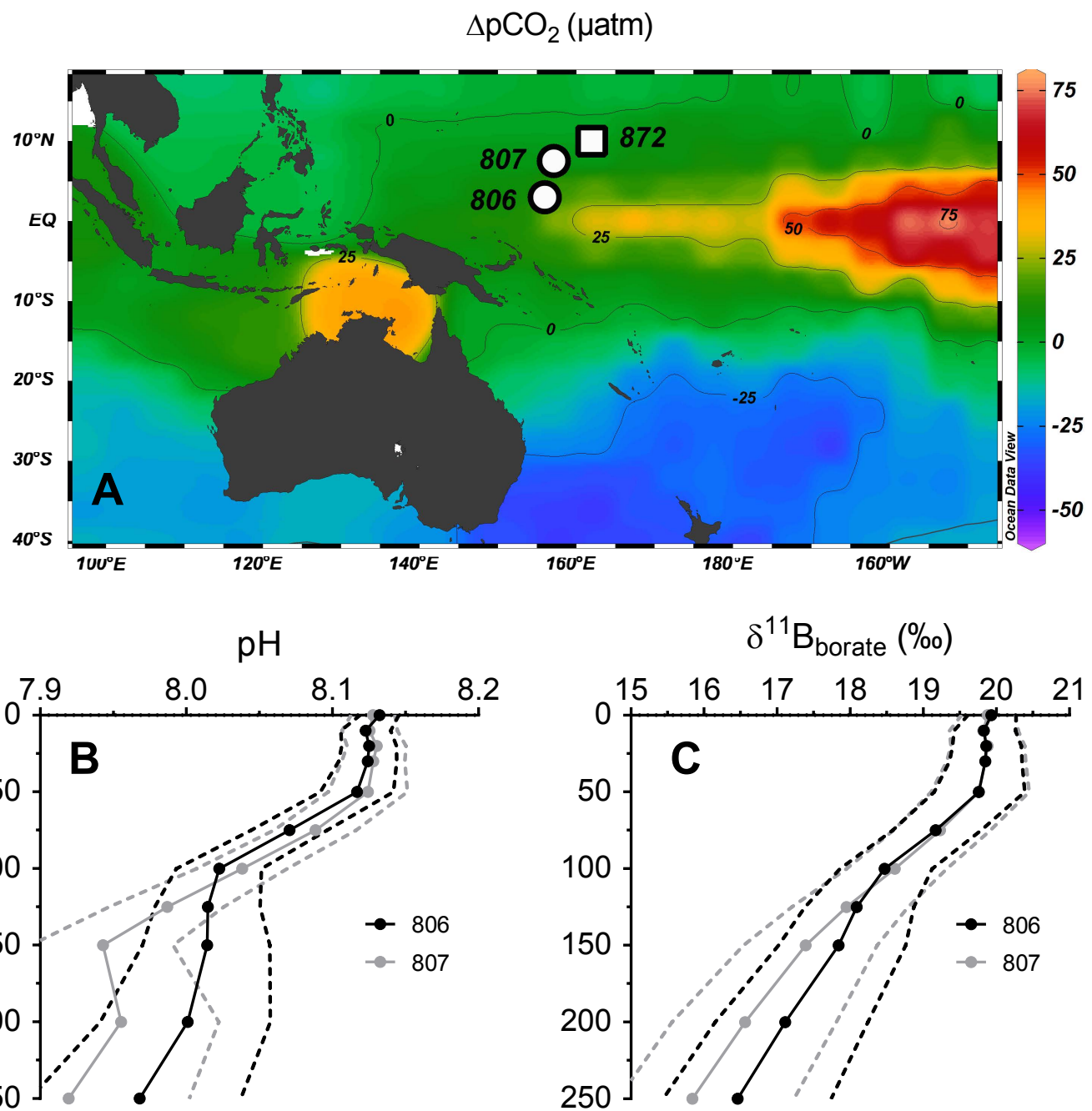


Figure 1

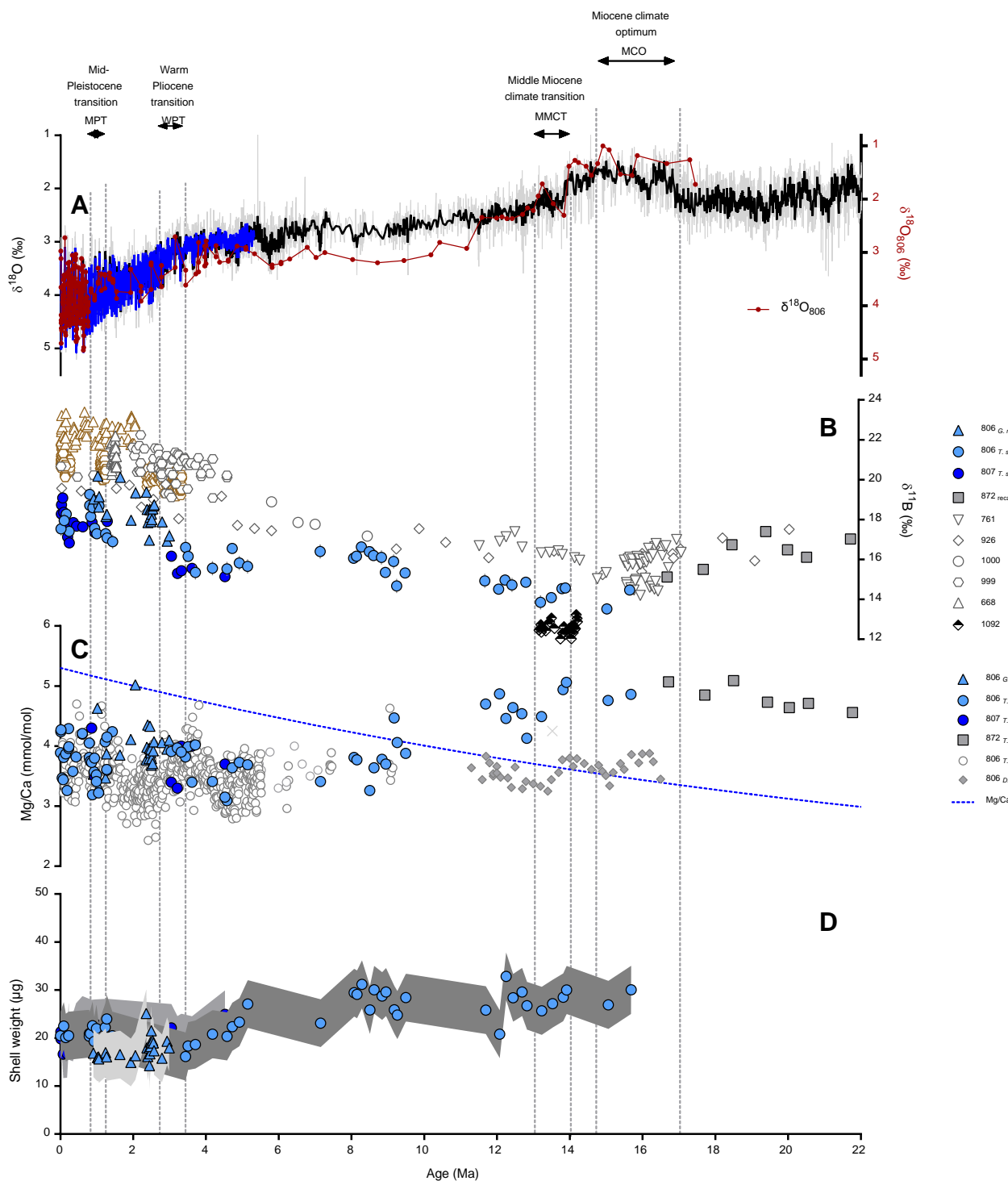


Figure 2

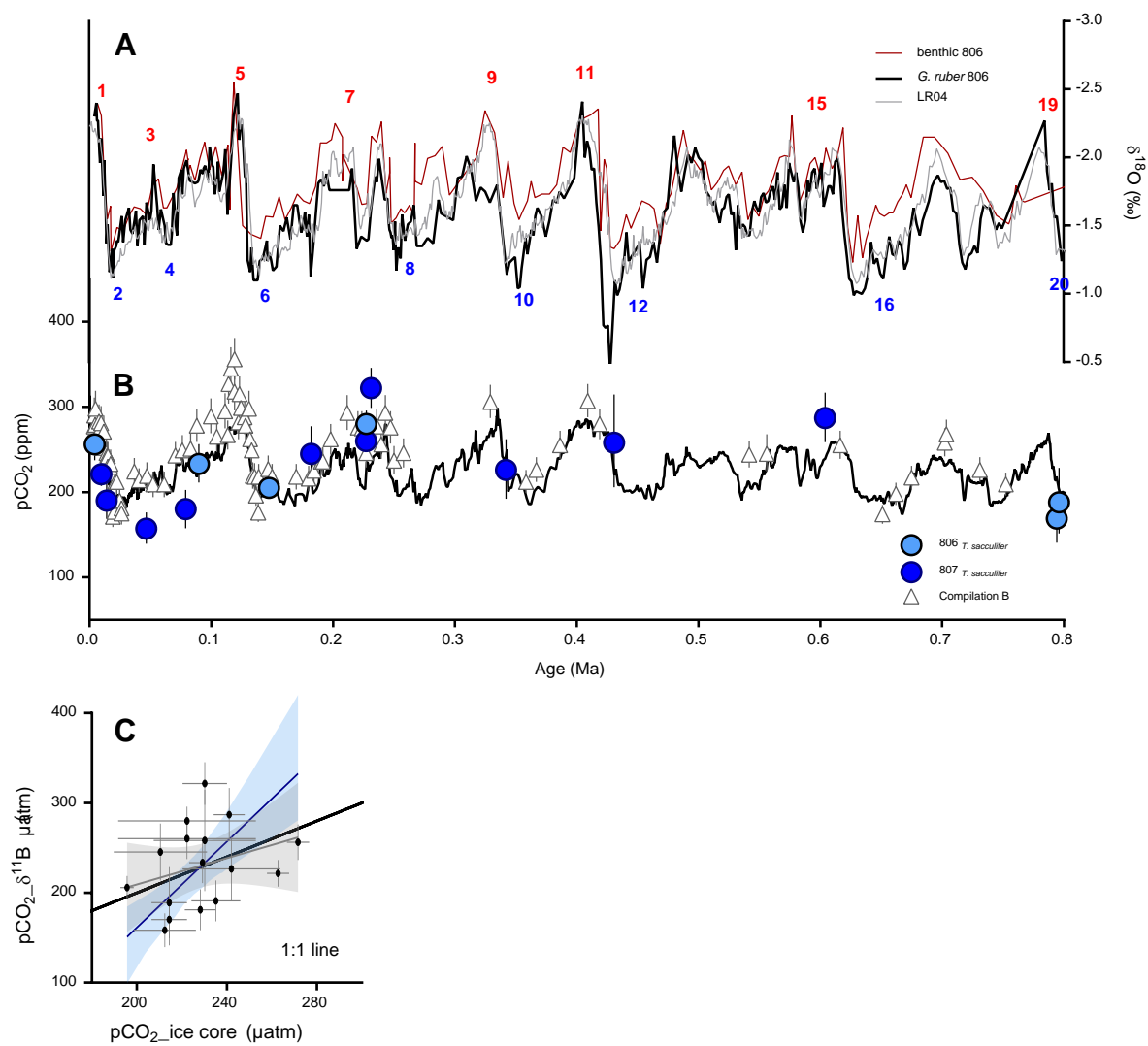


Figure 3

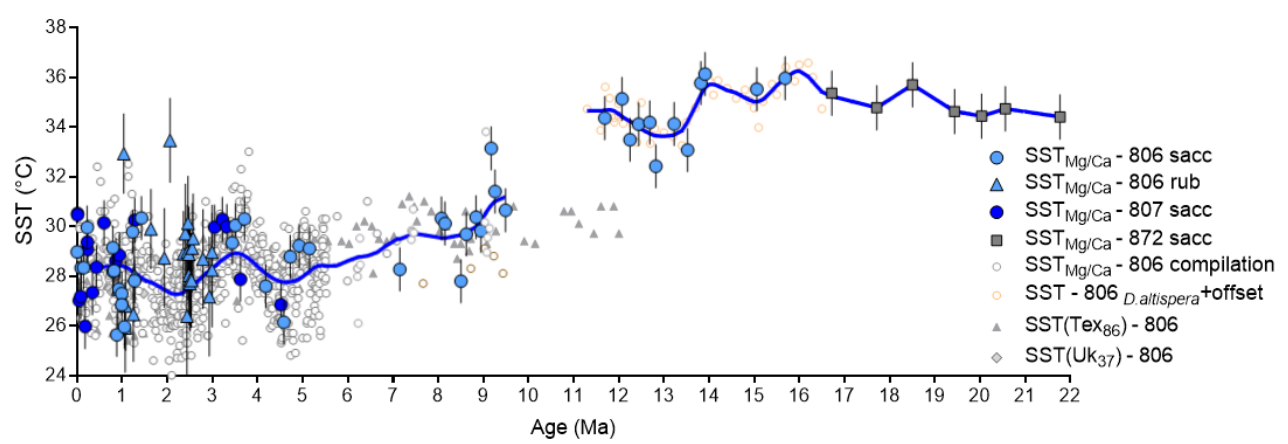


Figure 4

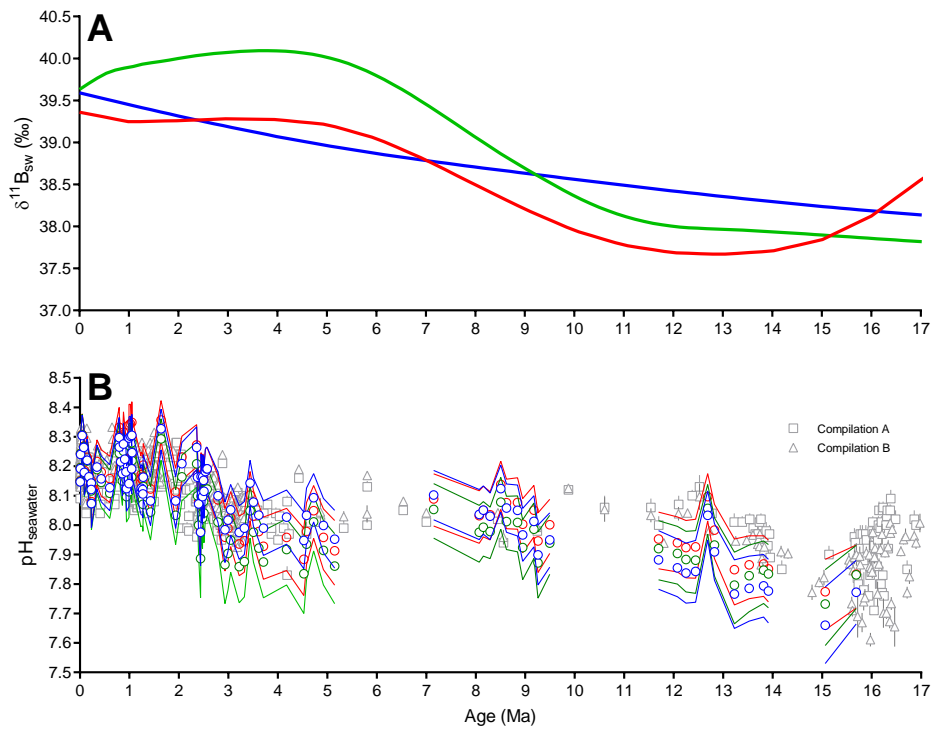


Figure 5

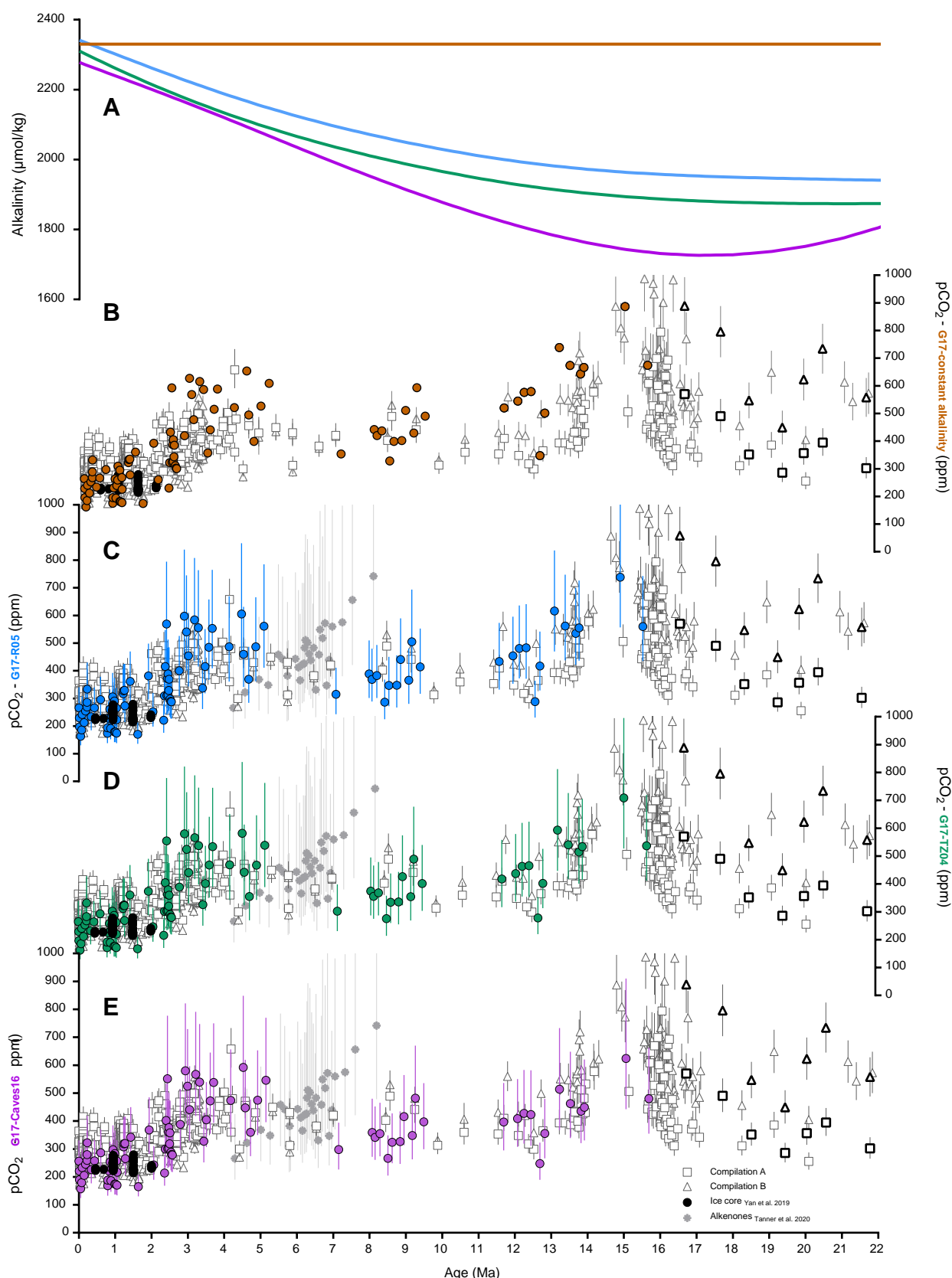


Figure 6

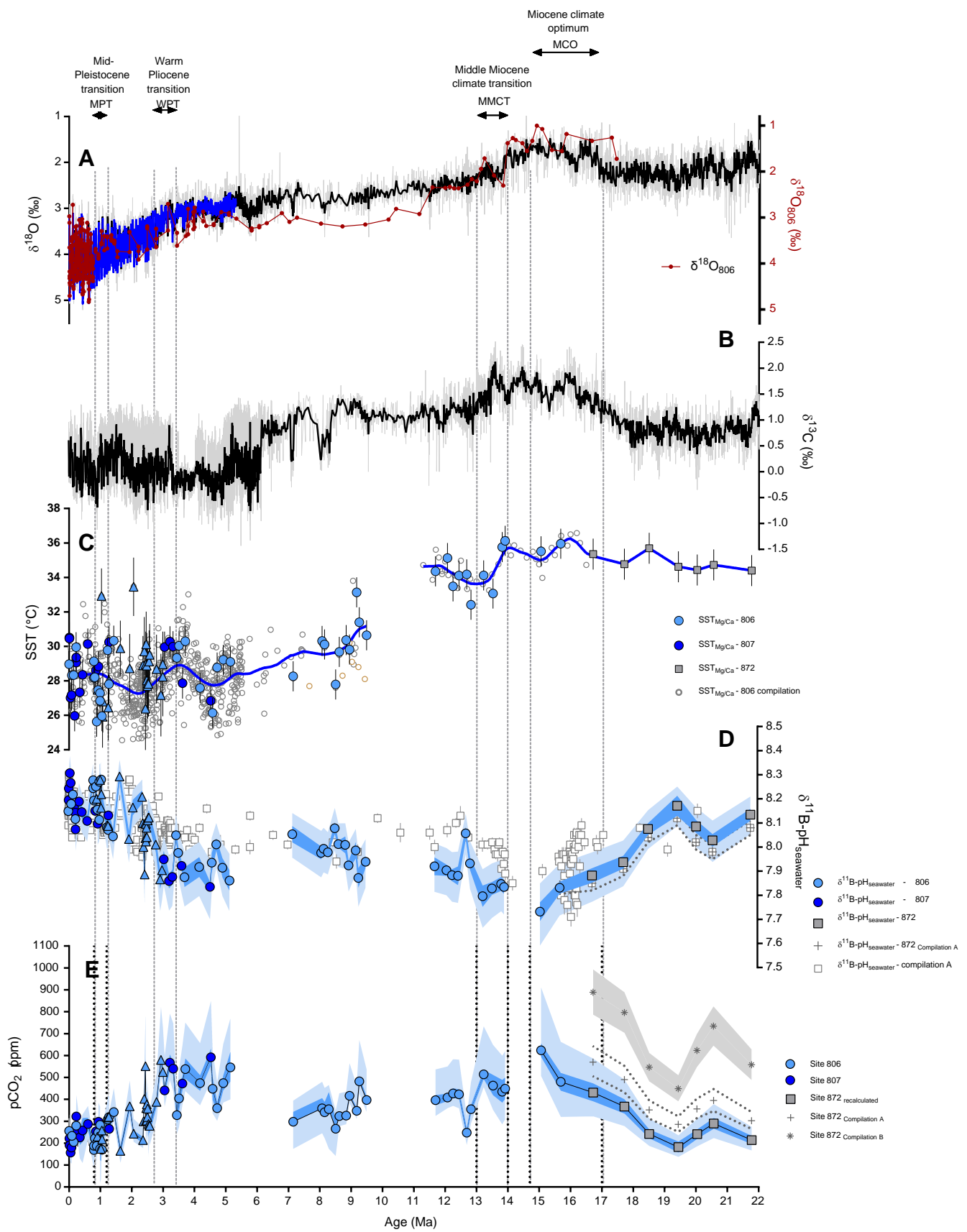


Figure 7

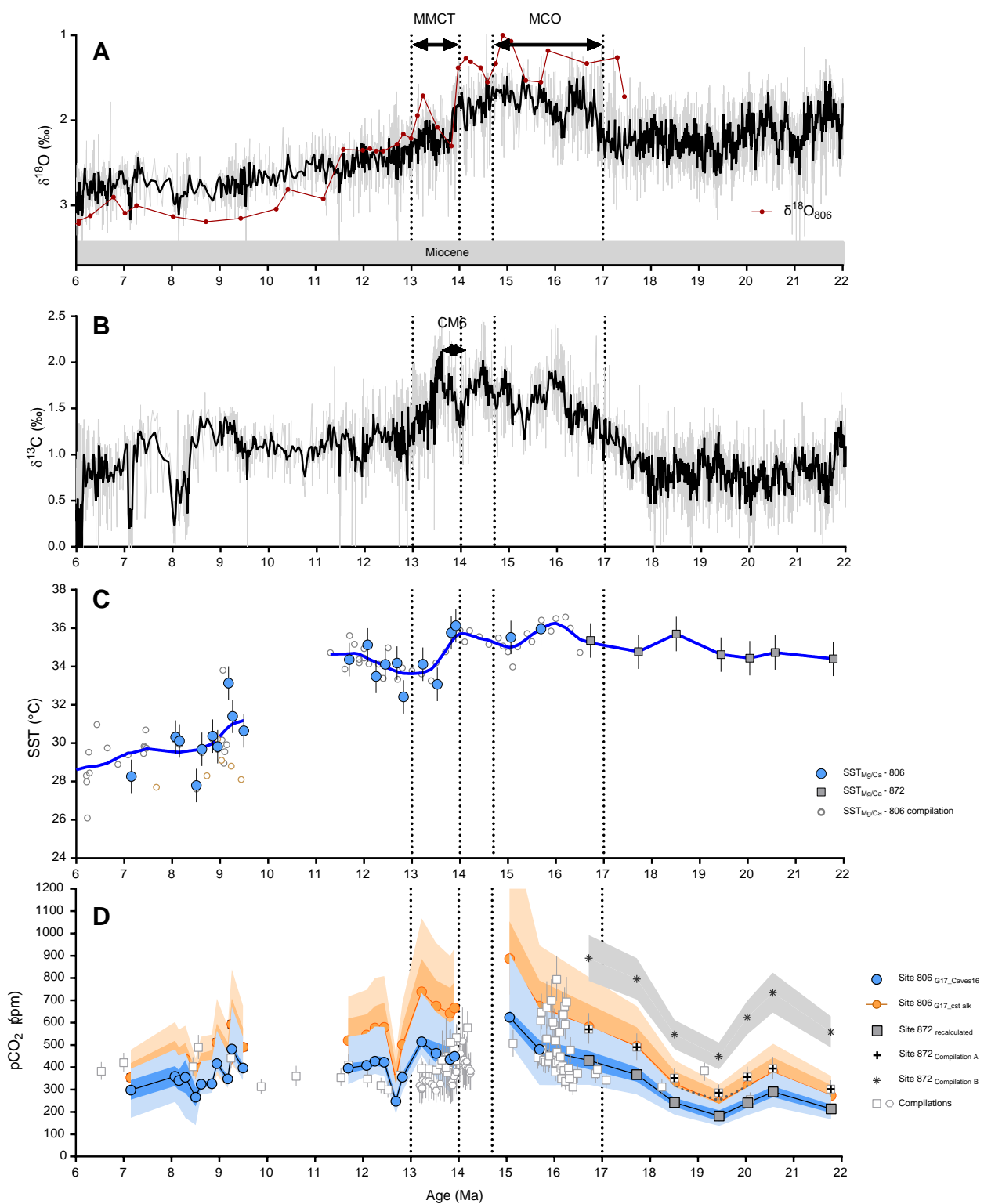


Figure 8

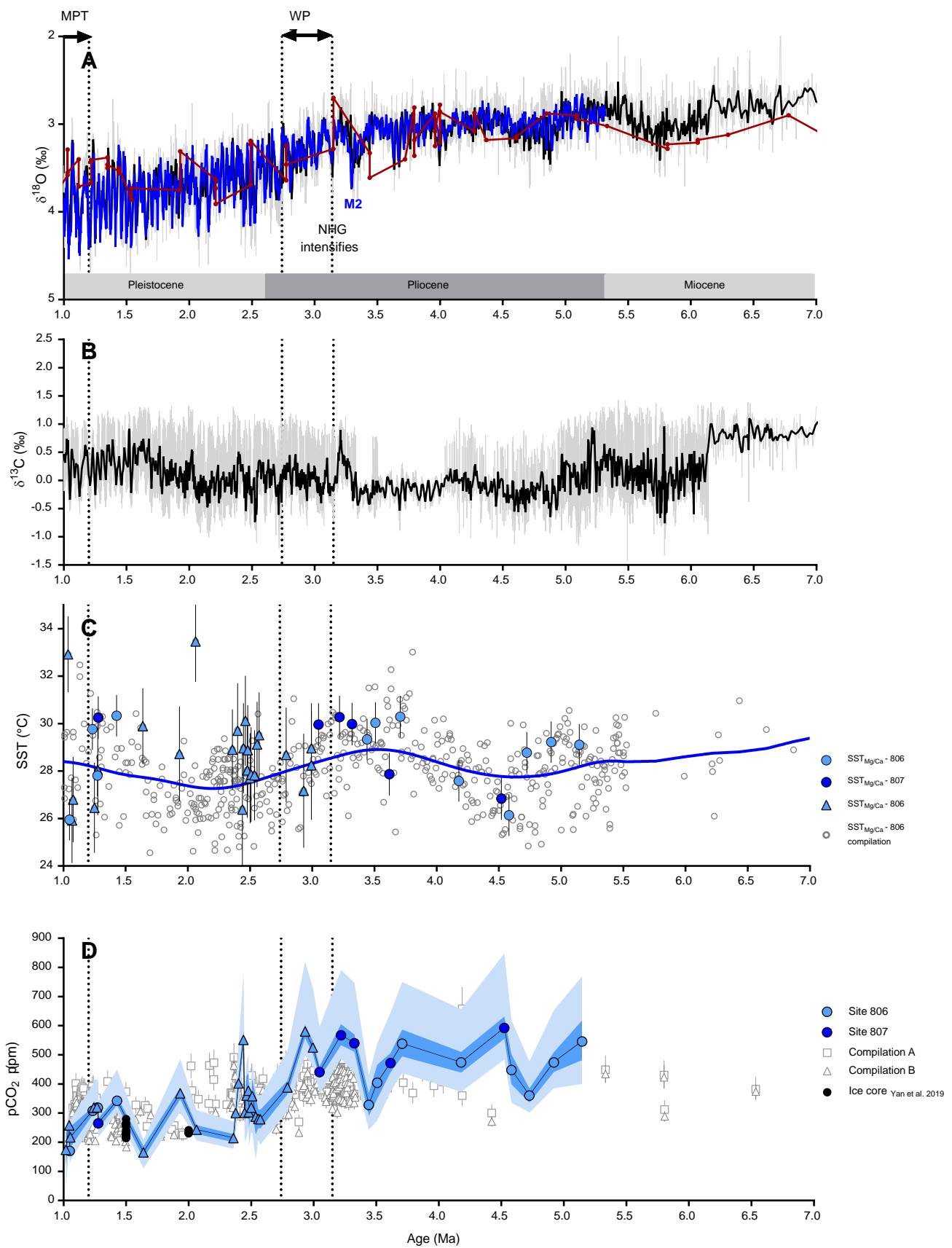


Figure 9

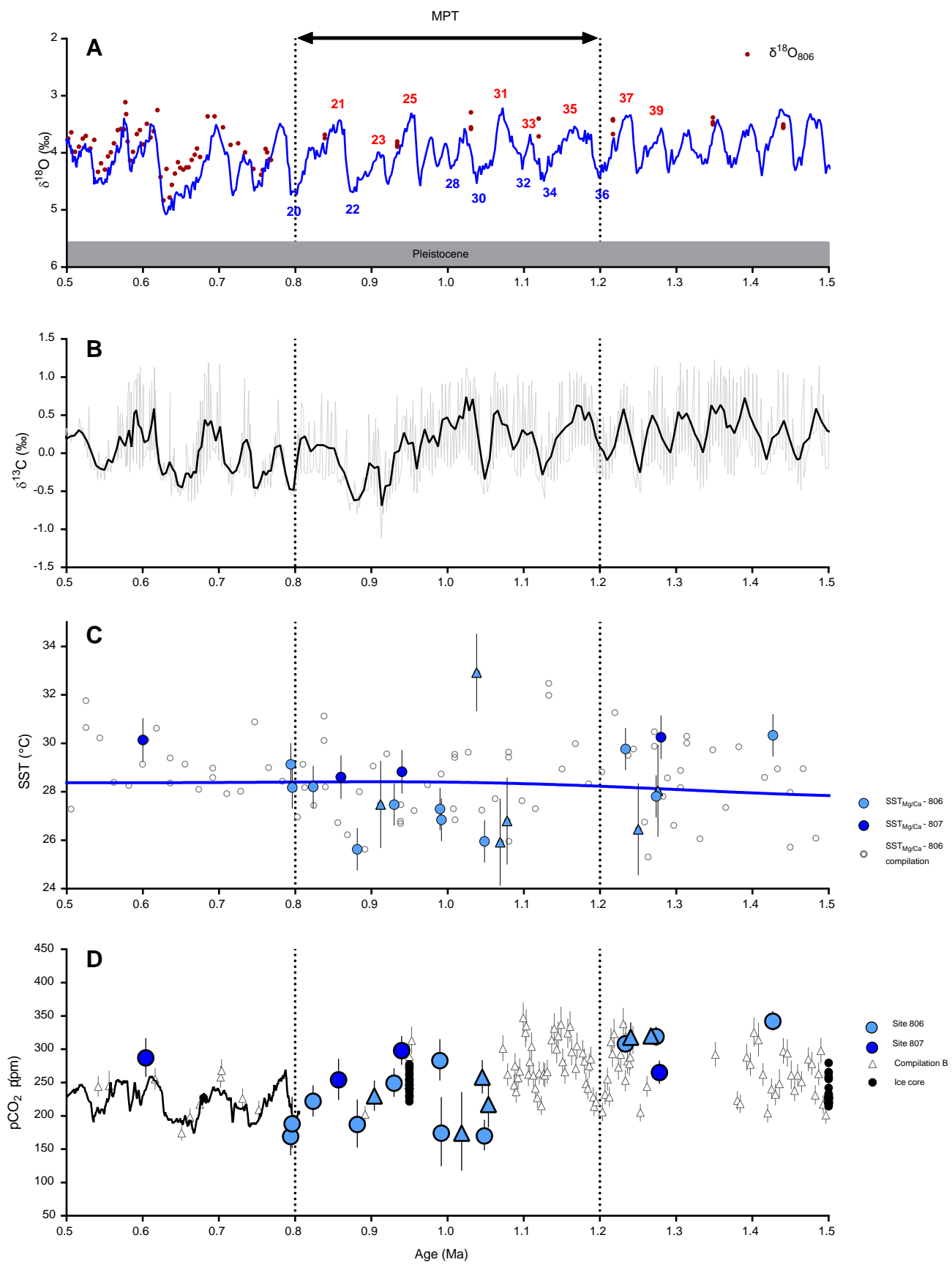


Figure 10

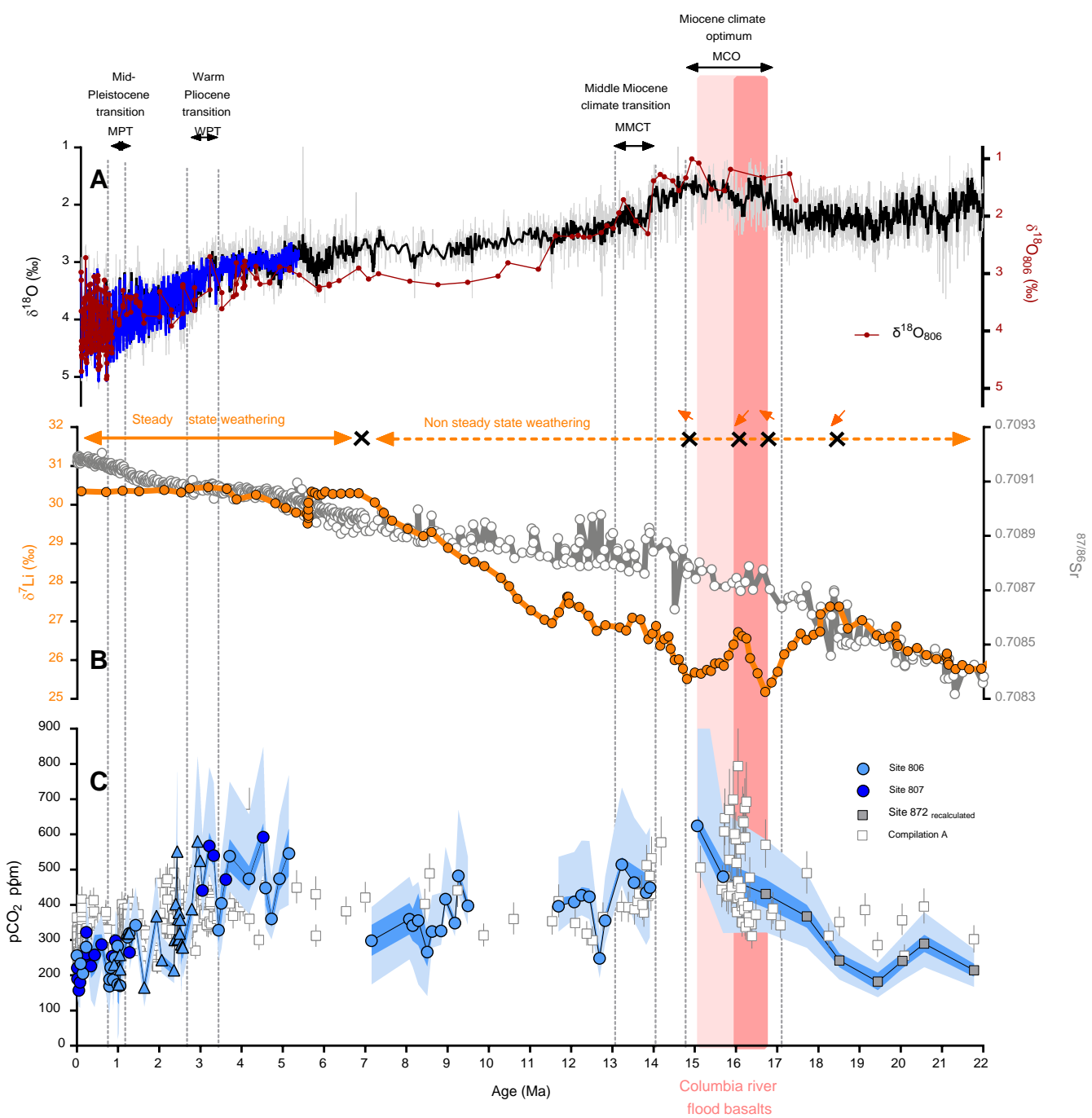


Figure 11